Master's thesis

NTNU
Norwegian University of Science and Technology
Faculty of Engineering
Department of Civil and Environmental Engineering

Magnus Leikvoll

On the Feasibility of Real-time Sea Level Monitoring using Ground-based GNSS-Reflectometry Measurements

Master's thesis in Engineering and ICT
Supervisor: Hossein Nahavandchi, Mostafa Hoseini
June 2020

NTNU
Norwegian University of
Science and Technology

Magnus Leikvoll

On the Feasibility of Real-time Sea Level Monitoring using Ground-based GNSS-Reflectometry Measurements

Master's thesis in Engineering and ICT
Supervisor: Hossein Nahavandchi, Mostafa Hoseini
June 2020

Norwegian University of Science and Technology
Faculty of Engineering
Department of Civil and Environmental Engineering

NTNU
Norwegian University of
Science and Technology

NTNU
Geomatics

Date
11.06.2020

Reference

TBA4925, Geomatics Master Thesis

Master Thesis
for
Magnus Leikvoll

Title:
On the Feasibility of Real-time Sea Level Monitoring using Ground-based GNSS-Reflectometry Measurements

Background:
GNSS reflectometry is an emerging remote sensing technique. This thesis will present the theory of GNSS-R altimetry using interferometric observations, and will present the results achieved through the use of real-time data stream to assess the possibilities of creating online reflectometry services.

The Student Will:
Present previous usages of the GNSS-R technology and provide the necessary theory for performing altimetry using GNSS-R. An experiment using GNSS-R will then be performed using an established GNSS-R station and perform altimetry using data received from the station. The accuracy, issues and limitations are discussed to assess the feasibility of using this method and data for the real-time application.

Administration:
The work on the Master Thesis starts January 15th, 2020
The thesis will be submitted digitally in INSPERA at June 11th, 2020 latest

Supervisors at NTNU:
Hossein Nahavandchi
Mostafa Hoseini

Abstract

Global Navigation Satellite Systems (GNSS) reflectometry (GNSS-R) is an emerging remote sensing technique with a vast area of applications. In this thesis we study the feasibility of real-time retrieval of sea level anomalies using a ground-based setup. To this end, we investigate the interferometric pattern caused by the interference of the signals received directly from the satellites with the signals reflected off the sea surface. The frequency of the interferometric signal is the main observable of interest. This observable is used to measure the height difference between the sea surface and the receiver antenna. The dataset used in this research consist of high-rate observations acquired from a ground-based experiment at Onsala space observatory in Sweden. A software package is developed in Python to handle the raw data stream from the receiver and pre-process the observations. In this study we focus on the measurements that are made from the stand-alone output data stream of the GNSS-R receiver with no external auxiliary data such as precise orbit information. Therefore, the broadcast ephemeris are used for retrieving satellite orbit information within the height estimation process. The height retrieval process is performed using the combination of the Singular Spectrum Analysis (SSA) and wavelet transform. A comparison of the retrieved heights with a nearby tide gauge measurements show promising estimates of sea level anomaly trends during favorable conditions. The favorable conditions are met when several satellites at low elevation angles can be tracked and used for the reflectometry measurements. Our investigation also highlights some of the limitations of the utilized observations and approach. The issues of availability of favorable satellites and the accuracy of the broadcast ephemeris can be considered as the major issues in this study. The study includes some suggested remarks about tackling the limitations and issues for future works.

Sammendrag

GNSS Reflektometri (GNSS-R) er en fjernmålingsteknikk som har fått mye oppmerksomhet i nyere tid. I denne avhandlingen blir teorien bak GNSS reflektometri presentert, og et eksperiment er gjennomført for å vurdere mulighetene til å bruke denne teknologien for sanntidsmålinger av tidevann og vannstand. Høyder er estimert ved å benytte signalene og efemeridene som blir sendt med dette signalet, hvor frekvensen til det interferometriske mønsteret mellom det direkte og det reflekterte signalet blir brukt for estimeringen. Data er hentet fra en mottaker i Onsala, Sverige, som leverer observasjoner med en frekvens på 200 Hz. Et python-script er laget for å håndtere rådata fra denne mottakeren og gjøre nødvendig pre-prosessering. Forsøket blir gjennomført ved å kun benytte data fra mottakeren, som medfører at vi bruker efemeridene som blir sent med gps-signalet i stedet for med nøyaktig omløpsinformasjon. "Singular Spectrum Analysis" og "Wavelet Analysis" blir brukt for å estimere høydene. Høydene blir så sammenlignet med en tidevannsmåler i nærheten av mottakeren. Vi observerer at vi har bedre resultater når vi kan gjennomføre altimetri med flere satelliter nær horisonten. Vi ser også flere begrensninger med metoden brukt. Tilgjengeligheten av satelliter og nøyaktigheten til omløpsinformasjonen brukt blir presentert som de mest begrensende faktorene. Forslag til mulige forbedringer for å redusere disse feilene blir også presentert.

Preface

This thesis is a completion of a Master of Science in Engineering and ICT with a specialization in Geomatics at the Norwegian University of Science and Technology (NTNU).

The subject of this thesis is new to the geomatics department at NTNU. Therefore, it has not been a part of any course during the semesters leading up to the writing of the thesis. A large emphasis for this thesis has therefore been put on learning and presenting the theory and concepts related to the subject.

I would like to thank my supervisors, Hossein Nahavandchi and Mostafa Hoseini, for their help and willingness to assist me with the issues that was encountered during the writing of the thesis. Their knowledge and enthusiasm for the subject have greatly helped me in both understanding the theory which had to be learned for this thesis as well as providing great advice throughout the entire process.

I would also like to thank my friends and family who have supported my endeavours throughout the final semesters. I would not have been able to complete my degree without your support and help.

Contents

List of Figures

List of Tables

Acronyms

ADC Analog to Digital Converter.

AGC Automatic Gain Control.

BCRS Bistatic Radar Cross Section.

C/A Coarse Acquisition.

dBWi Isotropic Decibel Watt.

DDM Delay Doppler Map.

GNSS Global Navigation Satellite System.

GNSS-R GNSS Reflectometry.

GPS Global Positioning system.

KA-GO Kirchhoff Approximation - Geometric Optics.

LEO Low Earth Orbit.

LHCP Left Handed Circular Polarized.

MSS Mean Square Slope.

PCA Principal Component Analysis.

PDF Probability Distribution Function.

PRN Pseudo Random Noise.

RF Radiowave Frequencies.

RHCP Right Handed Circular Polarized.

SNR Signal to Noise Ratio.

SPS Standard Positioning Service.

SSA Singular Spectrum Analysis.

SVD Singular Value Decomposition.

TFSR Tapped Feedback Shift Register.

1 Introduction

Over the last decades, the use of Global Navigation Satellite Systems (GNSS) has become more common. The primary function of these systems has for a long time been to provide an accurate positioning and timing service globally [Mai, 2012]. This service is provided based on the L-band signals generated with known structures in each satellite sent towards the Earth.

Several constellations are currently operational and maintained by different authorities. The Global Positioning System (GPS) is maintained and distributed by The American government, and aims to provide services for both civil and military purposes. In February 2020, GPS consisted of 31 operational satellites in 6 orbital planes [Force, 2020a]. GLONASS is distributed by the Russian authorities, and works very similarly to the American GPS with some distinct differences. From 2012, GLONASS was planned to consist of 24 satellites in 3 orbital planes [IAC, 2020]. Galileo is a created by the European Union, and is designed for civil purposes only. Its constellation is not yet fully complete, but the satellites were made available for public use in late 2016. The main motivation behind Galileo was to provide a positioning service for the EU members which was independent of the American and Russian authorities [GSA, 2019]. Currently, there are 26 Galileo satellites in orbit, which enables us to perform positioning tasks with its constellations. Several other positioning services exist, such as the Chinese controlled BeiDou, the Japanese QZSS and the Indian NavIC.

Receivers on or near the Earth's surface can utilize the available information about the structures and frequencies to capture the signals and be able to calculate their positions through trilateration. The GNSS currently offers near-global coverage. Additionally, the technology required for utilizing the GNSS satellites is very cheap. This is one of the main motivations for finding new applications of this technology. One of these new applications is the use of GNSS in *remote sensing*.

Remote sensing is the process of observing qualities of an object without interacting directly with it [Horning, 2008]. This can be achieved through measuring some signal coming from the object, both reflected and emitted.

For our purpose, this signal will be an electromagnetic signal reflected off the ocean surface. Several different techniques have been developed and remote sensing is widely used today to monitor several aspects of the Earth, such as variations in ice sheets [Shamshiri et al., 2018] and effects of earthquakes [Suresh and Yarrakula, 2019]. Another emerging remote sensing technique, is *GNSS reflectometry*. Cardellach et al. [2011] present several applications of this remote sensing technique, such as ice/snow monitoring, hydrology, soil moisture retrieval, vegetation detection, sea level determination and many more.

The main principle of *GNSS reflectometry*, or *GNSS-R* is to observe the signals reflected off a surface and use the properties of the received signal to infer information about the surface in consideration [Rius and Cardellach, 2017]. Figure 1 illustrate the principle for observation acquisition using the GNSS-R method. It is possible to obtain these measurements as the receiver acts as a bistatic radar, meaning that the receiver and the satellite are far apart from each other [Rius and Cardellach, 2017]. In contrast with the active radar, the GNSS receivers listening for signals sent from the satellites can be considered as passive sensors. This aspect of GNSS-R technique can make it a feasible choice for several applications.

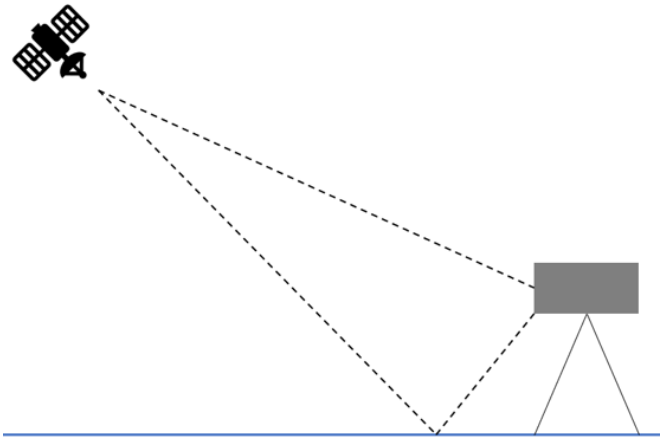

Figure 1: The main principle of reflectometry. The signal hitting the ground will be reflected towards the receiver. By observing the direct and the reflected signals, we aim to derive useful information about the surface

A passive reflectometry and interferometry system using the reflections

of GPS signals was presented by Martin-Neira [1993]. He proposed a method to perform altimetry over the oceans using the available signals of opportunity. The presented algorithm utilizes both the direct and reflected signals to perform the altimetric measurements with a scientifically acceptable level of precision. Garrison and Katzber [1998] set up an experiment with a specialized receiver to be able to read the signals scattered from the ocean surface. He also observed how changes in altitude of the receiver and the sea surface roughness affected the power of the received signals. It does however struggle to correlate the received signals with any physical phenomenon. Several later experiments managed to demonstrate the potential application areas, such as soil moisture determination [Rodriguez Alvarez et al., 2009] and ice/snow thickness [Cardellach et al., 2011].

From the experiments conducted so far, the scenarios considered for acquiring data can be generalized into four main groups. These are *ground based setups*, *shipborne campaigns*, *airborne experiments* and *spaceborne missions*.

In a ground-based configuration, the receiver is installed on the ground. The scope of such setups are often consist of observing some local phenomenon, as the area of coverage is limited. These experiments are usually static and therefore experience a slower changes in the satellite-receiver dynamics. Furthermore, it is possible to observe an area for a long and continuous period, which enables researchers to analyse geophysical parameters under different circumstances. Liu et al. [2017] for example used a ground-based experiment to measure the sea surface height under different sea surface states. Larson et al. [2008] on the other hand used a ground-based experiment to identify the soil moisture variations in the upper parts of the ground.

In a shipborne mission, the receiver is mounted on a ship which traverse an area of interest to observe some phenomenon. The dynamic movement of ships are to be considered in such experiments, and can prove challenging for data retrieval. However, compared to the ground-based configuration, the shipborne experiments allow for data retrieval over a larger area of interest. An example of a shipborne mission was presented by Semmling et al. [2019] who utilized a shipborne setup to measure the sea-ice concentration in the area between Greenland and Svalbard.

Airborne missions are performed using a variety of methods. Similarly to other airborne remote sensing techniques, drone or aircraft missions are commonly used to gather data, where the receiver is mounted on the vehicle to observe the desired area. compared to the ground based method, these

missions are generally used to observe larger areas, where the ground based experiments would observe a small area close to the receiver. Furthermore, more issues arise regarding noise levels due to various elements such as the movement of the aircraft and wind perturbations. Atmospheric effects also has to be taken into account, as the reflected signal is significantly more affected by atmospheric distortions compared to the direct signal [Liu et al., 2017].

In spaceborne missions, data is acquired from Low Earth Orbiting (LEO) satellites. These satellites can be considered to continue the observations over long periods, similar to ground-based observations but with a global coverage. Furthermore, the spaceborne missions can be used to detect more large-scale phenomenon as the satellites orbit around the Earth. Hoseini et al. [2020] for example used the CYGNSS satellite mission to characterize eddies found in the pacific ocean. Similar to airborne missions, the range differences between the direct and reflected signal is large, which causes atmospheric effects to be a significant source of error. It is therefore important to be able to model these errors well [Liu et al., 2017].

Several satellite missions have GNSS-R sensors onboard aiming to utilize this technique to remotely observe geophysical phenomena. As GNSS-R is a relatively new remote sensing technique, new potential applications are presented frequently. The potential for research of GNSS-R is further increased by the fact that these missions have made their data products publicly available. This policy has greatly reduced the entry barrier to the field of study. Dunbar and Allen [2017] emphasizes that the active GNSS constellations with ubiquitous signals makes the GNSS-R observations globally available. Moreover, specific features of the sapceborne GNSS-R, e.g. spatiotemporal resolution and revisit time, highlights this technique besides other remote sensing techniques. This can also increase the coverage and availability of scientific data products for the applications demanding timely data stream, e.g. Tsunami or flood early warning systems.

CYGNSS is a satellite mission launched by the American space agency (NASA), and aims at measuring wind speeds over the ocean. This constellation of micro-satellites are intended to improve the detection and research of hurricanes [Dunbar and Allen, 2017]. The data products of this mission at different levels are publicly available, and has inspired researchers to find new areas in which GNSS-R can be used. Besides the monitoring of hurricanes, Ruf et al. [2018] presented other applications of CYGNSS dataset where the GNSS-R measurements are used to map several geophysical aspects, such

as large rivers, flooding events and soil moisture. Kim and Lakshmi [2018] further used the data in combination with several other datasets to estimate the soil moisture. In addition, Hoseini et al. [2020] tried to use the CYGNSS data to characterize the responses created by ocean eddies.

A ground based experiment is conducted to observe the sea level at Onsala in Sweden. Data is gathered from a permanent receiver station at Onsala. The experiment will apply methods used in previous studies to be able to retrieve the observables necessary for the height determination. To do this, the necessary theory is presented and explained to enable reasoning for the observed results and intuition for the observations. Factors affecting the signals used for reflectometry, and their relevance for our purposes will be presented. Factors affecting the reflections and the different types of reflection used to model the reflections will also be presented. Afterwards, the instrumentation and processing methods are presented and described, as well as the data used for the computations. Lastly, the obtained results will be presented and discussed, which will assess the viability of the applied methods and data for use in real-time reflectometric applications.

2 Background and Theory

This section includes a brief introduction to the theoretical foundation and different factors involving in GNSS-R technique as needed in the scope of this thesis. The readers are referred to the references cited within this chapter for further detailed information. The concepts discussed in this chapter is based on the characteristics and specifications of GPS, the US global positioning system. However, the technique could generally exploit all the signals from the GNSS constellations in service.

2.1 Signal Specification

The signal generated by the satellite comprises of several components. The base component is the carrier wave, which is a sinusoidal wave with a frequency in the L-band spectrum. The carrier wave is then modulated with codes, which is used for several purposes such as satellite identification and range measurements, and a binary data message which contains useful parameters for data processing. This includes the ephemerides and the almanac. According to the official technical documentation released by the US government, signal specification for Standard Positioning Service (SPS) of GPS [1995], the ephemerides contain Keplerian orbital parameters and satellite time information. The ephemerides also contain information regarding satellite health, GPS week number, and the time the data was created. The almanac is also used to determine position. It is however much more coarse compared to the ephemerides. One of the main purposes of the almanac is to provide an estimate of orbital information of the satellites. The almanac has data which is valid for up to 90 days, enabling the receiver to more quickly lock onto the satellites.

Jin et al. [2014] expresses the general GPS signal as:

$$Y(t) = A(t)C(t)D(t)cos(\omega t) \tag{1}$$

where $A(t)$ is the amplitude modulation function, which is often expressed as a function of the received power of the signal, $C(t)$ is the code modulation,

$D(t)$ is the data modulation and ω is the carrier frequency of the signal. According to this signal structure, receivers can extract the data messages from the signal provided that they could have the knowledge of the code sequences and the carrier frequency.

The codes are used for several important tasks. The first task is identification of a satellite. To be able to use the codes for identification, they have to fulfill two requirements. The first requirement is that each code must be unique so that no satellite can be mistaken for another one. Secondly, it is important that the codes does not correlate significantly with any other of the codes, independently of an arbitrary bit shift in the code. As we in general do not know exactly where in the code sequence we are before locking onto the satellites, it is important that the codes are different regardless of where in the code sequence we are. The codes therefore need to exhibit orthogonal behavior with respect to each other. In addition to using the codes for identification, it is used for range measurements. If the codes are to be used in the range measurements, an additional requirement is added to the structure of the codes. The code cannot have any significant correlation with itself, except for when the code is perfectly aligned. This is due to the fact that both the satellite identification and the range determination can be done by calculating correlation of the signal with locally generated codes which can be slided with different lags. By sliding the generated codes and finding the correlation peak, we can retrieve the signal of the target satellite and eliminate the contributions from other satellites. Associated bit shift (lag) with the correlation peak can be translated into the time delay and further into the satellite-receiver range. Figure 2 shows an exemplary GPS C/A (Coarse Acquisition) code which can only correlates with the same code. As we can observe, the correlation only has a peak when the two codes are aligned. Figure 3 shows the correlation between two C/A codes from different satellites, which shows no significant peaks.

Polarization of the transmitted electromagnetic waves from the satellites is an important aspect of the GPS signals. The signals transmitted from the satellites are Right Hand Circular Polarized (RHCP). Circular polarization implies that the magnitude of the sent signal is constant. The direction of the signal amplitude does however change as a function of time. A right hand circularly polarized wave means that this rotation follows a right handed system according to the laws of electromagnetism. Knowing the polarization of the waves is very useful as receiving antennae can be designed to mainly "observe" waves of a particular polarization type. Normal GPS receivers are

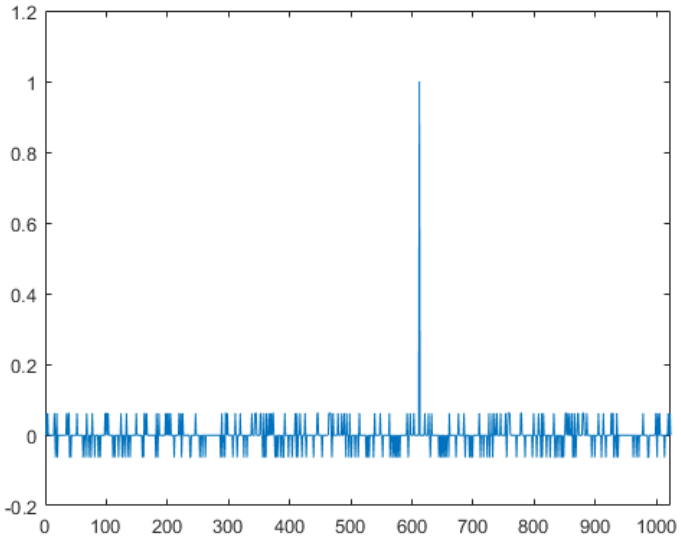

Figure 2: Correlation graph of a delayed C/A code with itself as a function of bit shift.

therefore most often RHCP receivers. In GNSS-R however, both RHCP and the left hand circular polarized (LHCP) versions are used.

To increase robustness and accuracy of the service for both civil and military users, each GPS satellite sends its messages over two or three *bands*, or carrier wave frequencies. All of these frequencies lie within what is called the L-bands, which range from around 1 to 2 GHz. According to Ogaja [2011], these frequencies are chosen for several reasons. First, it is important that they can reach the surface regardless of the weather conditions. Additionally, it is desirable to choose a set of frequencies which minimize the impact of atmospheric errors. This can be achieved by increasing the frequency of the signal. Finally, the frequency cannot be too large as GPS was created to accommodate small, low-cost receivers. If the frequency of the signal gets too high, it is necessary to use directional antennae to be able to read the signal. The L-bands can however be read by a small antenna. The L-bands were chosen as the best trade-off between the requirements.

The first bands used in GPS are L1 and L2. Both are defined as a base frequency $f_0 = 10.23MHz$ multiplied by an integer. The frequencies are defined as $f_{L1} = 154f_0$ and $f_{L2} = 120f_0$. L1 is usually considered the civil

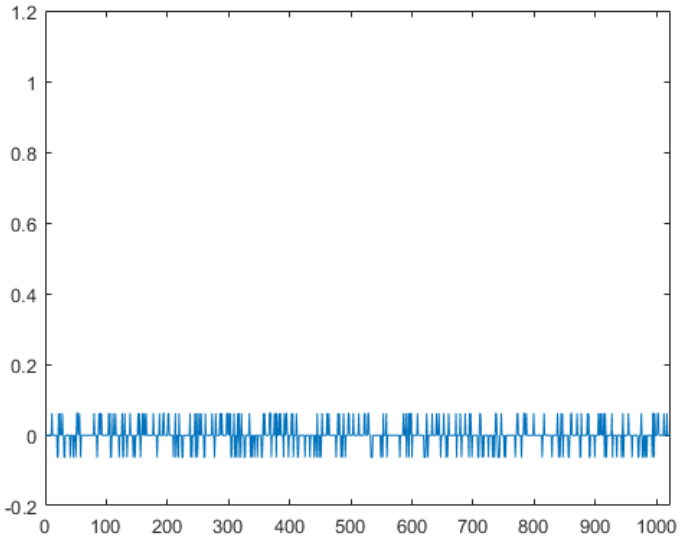

Figure 3: Cross correlation of two different C/A codes without any significant peak.

signal having both C/A and P(Y) codes modulated onto the carrier wave in quadrature. Jin et al. [2014] therefore extends Equation 1 to be:

$$Y(t) = A_P(t)P(t)W(t)D(t)cos(\omega_P t) + A_{CA}(t)CA(t)D(t)sin(\omega_{CA} t) \quad (2)$$

where $CA(t)$ is the modulation function of the civil PRN codes, $P(t)$ is the military P-code, $W(t)$ is an encryption modulation which encrypts the P-code. This is done to ensure that the military code is more resistant to spoofing.

L2 on the other hand is solely a military signal, and only has the encrypted P(Y) code modulated onto the carrier wave. Jin et al. [2014] defines the L2 signal very similarly to Equation 1 with defining it as:

$$Y(t) = A(t)P(t)W(t)D(t)cos(\omega t) \quad (3)$$

Several other bands are being supported by the newer satellites. These are L1C (L1 Civillian), L2C (L2 Civillian) and L5. These newer bands are intended to further increase the capabilities and robustness of the GPS [Force, 2020b].

2.2 Reception and Processing

Before we are able to utilize the GPS signals for reflectometric purposes, we are dependent on converting the received electromagnetic signal into a digital format. Several components are involved in this process, and the following paragraphs will explain the necessary steps in going from the received signal to the processed correlation output which will be used for further computations.

2.2.1 Antenna

The antenna is responsible for detecting electromagnetic waves and convert it to an electronic signal [Eissfeller and Won, 2017]. This electronic signal is in reality a voltage which is created by induction in the antenna caused by the electromagnetic waves [Media, 2007]. As we would optimally want to detect all satellites above the horizon, the antenna must be capable of detecting all satellites whose signal reach the antenna. However, as the signal travels through the atmosphere of the Earth, traditional antennas emphasize signal closer to zenith as the path through the atmosphere will be shorter for these signals, thus causing less distortion. These factors motivate the importance of the *antenna gain pattern*.

The antenna gain describe how much power is transmitted in a given direction compared to an isotropic source consuming the same power [Media, 2007]. The unit for gain is therefore noted as $dBWi$, or *isotropic decibel watt* to quantify the scale between an isotropic source and our antenna. While the definition of gain refers to the ability of the antenna to transmit a signal, we know that the transmit and receptive properties of an antenna are identical due to *reciprocity* [Neiman, 1943]. The antenna gain pattern is a plot of the antenna gain as a function of elevation angle. An example of this can be found in Figure 4. The figure shows how an antenna is designed to fulfill the previously mentioned criteria.

2.2.2 Receiver Front-end

The front end of the receiver refers to the part of the receiver which operates with an analog signal [Zolfaghari, 2003]. There exist several different viable architectures, such as the one found in Figure 5. This section will present different components which are usually present in a generic GNSS front-end

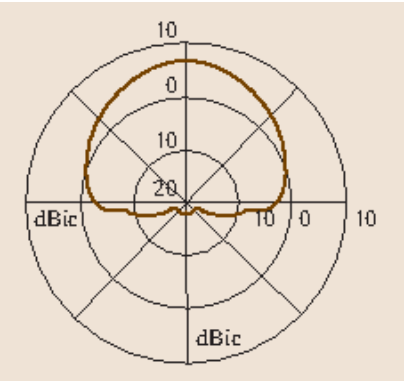

Figure 4: Example of a typical GPS RHCP gain pattern presented by Eissfeller and Won [2017]. We can observe that the gain is at maximum at zenith and gradually decreases as the elevation angle increases. For angles under the horizon, the gain is close to zero.

receiver and provide some reasoning for why these components are necessary for further processing of the received signal.

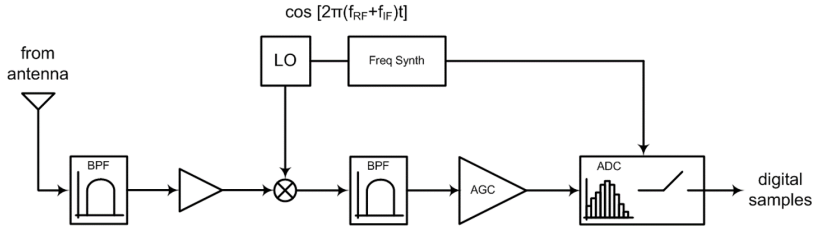

Figure 5: An example of a front end architecture as presented by Sarnadas [2011]

When the signal first comes from the antenna, the power of the signal is very low. As every step in the signal processing introduces some noise, we would prefer to have the same signal at a greater power to ensure that the noise introduced has less impact on the overall signal. This is achieved by amplifying the signal using a *Low Noise Amplifier* (LNA). The main purpose of the LNA is to increase the power of the signal without significantly affect the signal to noise ratio of the signal. As noise is introduced when sending the signal from the antenna to the receiver, some architectures implements the LNA as a part of the antenna. We then refer to the antenna as an *active*

antenna [Eissfeller and Won, 2017].

After the signal has been amplified, the receiver applies certain filters to remove large noise contributors. These noise contributors come from the fact that the antenna cannot distinguish between the electromagnetic waves originating from the satellites and those that do not. The power registered by the antenna is a sum of all these received signals. It is therefore important to have good filtering rules to be able to find the relevant components. There are some commonly used designs for filters. One of these is to reject frequencies which we know are not part of the GPS signal. We can therefore reduce the range of the frequencies down to around $20MHz$.

Some filtering is also achieved during the antenna reception stage. This is due to the fact that the antennas are designed to detect a set range of frequencies. A common antenna will for example be much better at detecting a certain polarization type, while other polarizations will have a much lower reception power. Furthermore, the gain patterns of the antennas are often much lower for lower elevation angles, which eliminate signals coming from the ground. Finally, as the antennas are not directional, it is not capable of detecting low frequency signals, which filters out these frequencies.

The next step which done in front-end receivers, is a down-conversion of the signal. When going from an analog to a digital signal, we have to do a sampling process to be able to digitize it. The carrier waves have a frequency of around $1.5GHz$. If we were to sample this signal, we would have to have a sampling rate of over $3GHz$ due to the Nyquist-Shannon sampling theorem. If we were to sample at this frequency, the necessary components would be very expensive and require a lot of power to do so. To avoid doing so, the received signal is down-converted to a lower frequency using a *Local Oscillator*. This is done by producing the difference between the phases of the received signal and the locally generated signal which yields a lower frequency signal known as an *intermediate frequency*:

$$\omega_{IF} = \omega_1 - \omega_{LO} \tag{4}$$

where ω_{IF} is the intermediate frequency, ω is the received frequency and ω_{LO} is the locally generated frequency. This frequency will be much easier to sample as the end frequency will be significantly lower.

There are two main methods used for down-conversion. These are *homodyning* and *heterodyning*. In a homodyne down-conversion scheme, we only perform one donw-conversion process and sample the result of this one down-conversion. In a heterodyne down-conversion scheme however, the signal is

down-converted several times before it is sampled. The benefit of utilizing such a scheme, is that we are able to perform filtering rules at the different intermediate frequencies, which enables us to reject out-of-band frequencies very well [Eissfeller and Won, 2017]. This can be beneficial as we can observe different signal signatures at the down-conversion stages. As such, heterodyne down-conversion is the most common approach in receiver front-ends [Eissfeller and Won, 2017, Sarnadas, 2011]. Figure 6 shows an example of a heterodyne down-conversion scheme.

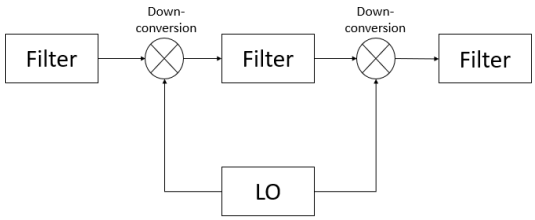

Figure 6: Example of a 2-step heterodyne down-conversion scheme. We apply a filter after each down-conversion step to remove noise components from the signal.

After the signal has been down-converted to a frequency which we can sample, we can start converting the analog signal to a digital one. This is done through processes known as *sampling* and *quantization*. Sampling refers to the process of going from a continuous time interval to a discrete one, while quantization refers to the process of going from a continuous set of possible values of the signal to a predetermined set of values. Both of these tasks are performed by a module called the *Analog to Digital Converter* (ADC).

Several aspects need to be considered for the design of the ADC. First, the sampling frequency has to be chosen such that we manage to represent the analog signal correctly. As we are going from a continuous domain to a discrete one, we will introduce what is known as *sampling loss*. In addition, one can differ between uniform and non-uniform sampling intervals. In a uniform sampling interval, each time step will be equal, while for non-uniform sampling this will not be the case. The uniform approach is the most common one. For quantization, the number of values which the analog signal can be assigned is dependent on the number of bits used to represent the signal. This conversion will introduce a *quantization loss*, similarly to sampling as we are going from a continuous domain to a discrete one. An increase in

bits used to represent signal values reduces the quantization loss, but also increase the copmlexity of the receiver.

During the quantization process, it is important that the thresholds set for the different values are chosen such that the signal falls in between the extremal thresholds of the ADC [Eissfeller and Won, 2017]. As the amplitude and power received can vary over time, it is therefore necessary to have this range decided dynamically to ensure that all range values are used optimally. This is achieved by using an *Automatic Gain Control* (AGC). The AGC is a feedback loop which works to adjust the quantization level thresholds. By doing this, the ADC is capable of having a greater dynamic range. In other words, it enables the receiver to digitize the signal both when the amplitude of the signal is large and when it is small.

2.2.3 Correlation

As described in Section 2.1, the signals sent from the satellites are designed to be able to both identify the satellite which is sending the signal, and enabling us to do range measurements. Figures 2 and 3 show the beneficial properties of the PRN code design which allows us to perform these tasks. This process is done after the received signals are digitized by the receiver front-end.

The correlation of codes are done by comparing the received code with a locally generated code. Initially, the receiver does not know which code it is reading. It is therefore necessary for this locally generated code to be changed several times until the correct code is found. This is achieved by using two *Tapped Feedback Shift Registers* (TFSRs). A shift register can be viewed as an array of bits where each bit gets shifted one place to the right between states. A TFSR is simply a shift register where the first bit in the array is dependent on the previous state through some linear function of the bit values. Figure 7 shows how the new bits are determined in the simplest of the two TFSRs for generating the C/A codes, which are 10-bit TFSRs. Here we can observe that the polynomial used to generate new input is given by

$$x_{new} = 1 + x_3 + x_{10} \tag{5}$$

The second TFSR works similarly to the first when generating C/A codes. However, the polynomial for generating new input bits is defined as:

$$x_{new} = 1 + x_2 + x_3 + x_6 + x_8 + x_9 + x_{10} \tag{6}$$

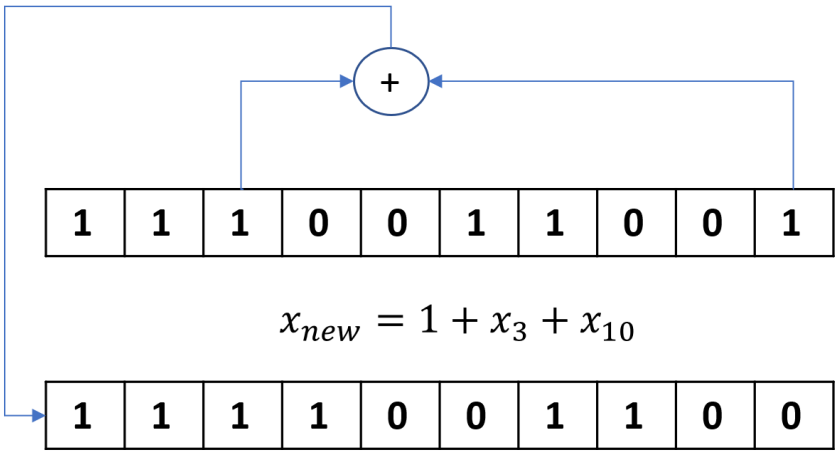

Figure 7: How a new bit is inserted into a TFSR based on its previous state. The output value from the defining polynomial is computed as modulo 2 to get valid numbers.

The codes are generated by reading certain bit values from both TFSRs. For the first mentioned one, the output bit (the one to be removed from the array) is used. For the latter one, the contribution is achieved through *taps*. The taps point at specific array indices and read these for the code generation. Which indices are read is dependent on which satellite we are considering and is what enables us to easily separate all satellites. As they both are 10-bit, the code sequence will repeat itself every $2^{10} - 1 = 1023$ bits, which is an important reason why the previously mentioned base frequency is $f_0 = 10.23MHz$.

In addition to the use of TFSRs to find correlation peaks, we also have to consider how the Doppler effect has affected the signal. The Doppler effect is a perceived change in frequency due to a relative speed difference between transmitter and receiver. As both the receiver and the satellite can be moving, they both have to be considered. While we cannot know the exact Doppler shift beforehand, we can determine the limits of its potential values. We know the GPS satellites move at a maximum velocity of around $14000km/h \approx 3900m/s$. The maximum relative velocity towards a fixed point on the Earth be when it just crosses the horizon of the satellite signal. This value can be computed as.

$$v_{rel} = v_{sat} \cdot \frac{R_E}{R_{sat}} \tag{7}$$

where v_{rel} is the velocity of the satellite relative to the point on the Earth, v_{sat} is the maximum velocity of the satellite relative to coordinates on the Earth, R_E is the radius of the Earth (around $6370km$) and R_{sat} is the distance from the Earth mass centre to the satellite (around $26500km$). By inserting these values into Equation 7 we get a relative velocity of $937m/s$. If we consider the L1 band, which has a wavelength of $19cm$, we get a potential maximum Doppler shift of $f_D = \frac{937m/s}{0.19m} = 4.2kHz$. This value of maximum Doppler shift enables the receiver to drastically reduce the size of the search space, as we know the shift cannot be greater than f_D.

2.3 Reflections

There are several ways in which the signal can be reflected off a given surface. This section will focus on presenting the different types of reflection, and what conditions must be met for the different types of reflections to occur.

One of the main types of reflection considered in litterature is *specular reflection*. Jin et al. [2014] define specular reflection as a mirror-like reflection. For specular reflections, a signal is reflected off a single point on a plane. For a given plane, the *specular point* of a signal is unique. The incidence angle with respect to the normal of the plane is also equal to the angle of reflection. Figure 8 illustrate specular reflection on a calm ocean surface. Each point on the ocean surface reflect a unique point, causing a mirror-like effect. If we assume a completely calm ocean surface, the signal from a GPS satellite will therefore yield a single specular point on the ocean surface which will reflect off the surface with a reflection angle equal to the elevation angle of the satellite.

In normal situations however, we cannot expect to be observing a smooth surface which is required for specular reflection. In reality, the surface will have a large variation in its slope. This motivates the concept of *surface roughness*. Surface roughness is a term used to describe how the signals hitting the surface will act on impact. It is often expressed through what is called the *mean square slope* (MSS), which is defined as the variance of the surface slope. If the MSS is low, the surface roughness is low. We would therefore have a relatively smooth surface and expect our reflections to be primarily specular. However, if we have a large MSS, this will not be the case. As the variance in the surface slope increases, we would experience that the specular point would not necessarily be where we would expect. This is caused by the fact that the surface slope causes the signal to be reflected

Figure 8: Image of Mount Hood released by the American Department of Transportation. The mountain is nearly perfectly mirrored by the reflection in the lake due to the dominant specular reflection coming from the clear water surface.

in different ways compared to the smooth case. The receiver may therefore receive signals from several different points on the surface as shown in Figure 9. When the reflections from the surface exhibit this more random nature, we call it *diffuse reflection*.

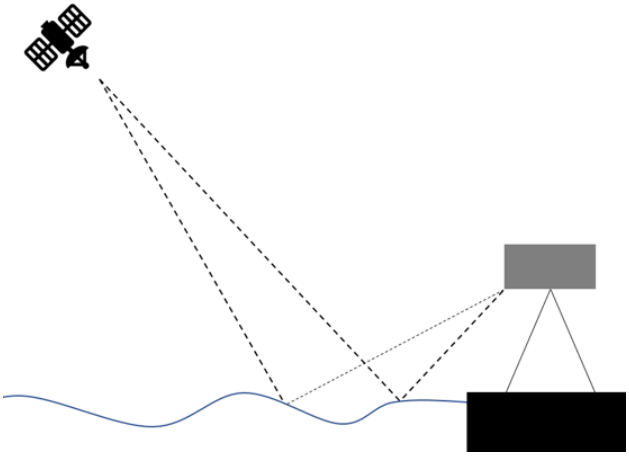

Figure 9: Concept of diffuse reflections. The signal arriving at the receiver are reflected from several different points on the surface.

When doing GNSS-R observations, we would not usually consider the received reflection as purely specular or diffuse. Rather, we consider the situation to be a combination of both. Dependent on the surface in question, the received signal can largely be dominated by one of the types. If we for example consider the ocean surface on a day with close to zero wind, we expect the MSS of the ocean surface to be low. The reflections would therefore be mostly specular. However, as the MSS would not be zero, some diffuse components would also be picked up by the receiver. If these components were considered as part of the specular component, the errors of the models would increase. How the different reflection types are modelled are explained further in Section 2.3.1.

Coherent reflections are closely related to specular reflections. When we receive a signal which is dominantly specular, we would not expect the specular point to move considerably. We would therefore expect the received signal to behave coherent. If diffuse reflections dominate the received signal however, this would not be the case. For diffuse reflections, the source of the signal is coming from several different points, and the contribution from each point varies over time. Due to this, the received signal will be incoherent.

2.3.1 Kirchhoff Approximation (KA-GO)

As we can observe, the environment we are trying to observe is very complex. It would be impossible to perfectly model all variations. We therefore need to create a model which simplify our world, but without sacrificing quality of output. The geometric optics limit of the *Kirchhoff Approximation* (KA-GO) is a model commonly used in GNSS-R. Ruf et al. [2016] and Zavorotny et al. [2014] provide derivations of the KA-GO definitions and formulas. The model aims to express the correlation power as a function of both code delay and doppler shift. The received signal used for this correlation power is considered to only come from *well oriented facets* [Jin et al., 2014]. A facet is for this purpose a continuous surface patch which is at least a few wavelengths in size, such that the signal can reliably be reflected off it. KA-GO also considers all reflections off these facets as specular. This assumption drastically simplifies our understanding of diffuse reflection, as we can assume all contributions originate from a specular reflection from the facets. A well oriented facet is a facet which is oriented in such a way that the reflected signal is directed towards the antenna.

Jin et al. [2014] considers where these well-oriented facets are located. It is important to identify where we would encounter them with some minimum probability. This area is often referred to as the *glistening zone*. This area is centered around the specular point of the hypothetical perfectly smooth surface, otherwise known as the *nominal specular point*. The size of the glistening zone depends on the surface roughness and the height of the receiver antenna. In mathematical terms, the glistening zone is often expressed through the use of the *Normalized Bistatic Radar Cross Section*, which is described more in detail in Section 2.4.

If we assume a purely diffuse scattering regime, ie. the specular reflection is ignored, the correlation power is computed using the following formula:

$$\langle |Y(\tau, f)|^2 \rangle = \frac{\lambda^2 T_i^2}{(4\pi)^3} P_t G_t \int\int \frac{G_r}{R_t^2 R_r^2} \chi^2(\tau, f) \sigma_0 dS \tag{8}$$

where τ is the chip delay, f is the Doppler shift, T_i is the coherent integration time, $P_t G_t$ is the effective isotropic radiated power, G_r is the gain pattern of the receiver, R_t and R_r are the ranges between the nominal specular point and the satellite and receiver respectively. χ is the ambiguity function. The ambiguity function is introduced as we may observe high correlation peaks at a given τ, f which are falsely identified as a given point [Li and Kiang, 2005]. This is caused by the fact that we may observe similar correlation levels for two different delays and Doppler shifts due to other noise contributors. σ_0 is the previously mentioned normalized bistatic radar cross section.

While Equation 8 expresses the correlation caused by diffuse reflections, we would in most cases have a non-negligible specular reflection coming from the nominal specular point. This component must also be taken into account. Zavorotny et al. [2014] define the specular correlation component as:

$$\langle |Y(\tau, f)|^2 \rangle_{spec} = |Y_0(\tau, f)|^2 |\Re| exp(-8\pi^2 \sigma_h^2 cos^2 \Theta / \lambda^2) \tag{9}$$

where $|Y_0(\tau, f)|^2$ is a mirror of the direct signal, $|\Re|$ is the Fresnel reflection coefficient. The equation will have its maximum at the delay and Doppler of the nominal specular point, which is to be expected as it models the specular reflection. This term is then added to Equation 8 to consider both specular and diffuse contributions.

2.3.2 Temporal Coherence

As part of the receiver workflow the received signal is down-converted from radio-wave frequencies (RF) to intermediate frequencies (IF). This is done

through subtracting the received signal with a locally generated replica. However, this locally generated replica has to estimate certain parameters, such as the Doppler shift. Due to small errors in our estimation of these parameters, interferometric patterns occur when computing the temporal coherence. This motivates the necessity for considering *coherent* and *incoherent* time intervals.

Temporal coherence is defined as the average correlation for a wave at a given lag τ over a time period t. When computing the temporal coherence between the locally generated signal and the received signal, we therefore try to find the τ of maximum correlation. However, as previously mentioned, we will have some small differences in the wave. Over long time periods t, we can therefore observe incoherent behavior although we would expect them to be coherent. However, over shorter time intervals the waves are expected to behave coherently. Rius and Cardellach [2017] define the temporal coherence as:

$$Y_{RD}(t_c, \tau) = \frac{1}{T_c} \int_{T_c} V_R(t+\tau) V_D^{c*}(t) dt \tag{10}$$

where V_D^{c*} is the complex conjugate of the direct time compensated signal samples, V_R is the reflected signal samples and τ is the time delay. Due to the incoherent nature over longer time intervals, it is important to choose a time period T_c small enough for the waves to be coherent. In the method presented by Rius and Cardellach [2017] a coherent integration interval of $1ms$ was used.

Rius and Cardellach [2017] also introduced an incoherent averaging interval to reduce certain noise contributors such as thermal and speckle noise, This incoherent averaging method was defined as:

$$W_{RD}(t_a, \tau) = \langle |Y_{RD}(t_c, \tau)|^2 \rangle_{T_a} \tag{11}$$

where W_{RD} is the received waveform, T_a is the incoherent averaging interval, and $\langle f(x) \rangle_T$ denotes the average value of $f(x)$ over time period T. By averaging a set of coherent observations, the aim is to reduce local temporal variations caused by the noise sources. In comparison to the coherent time interval T_c, T_a can be much larger, often up to several seconds.

2.4 Observables

The main output of the receiver is the received signal at different time slots. These measured voltages are then translated into a digitised signal which

we can use for performing the necessary tasks. This process is discussed in more detail in Section 2.2.2. The time delay is computed from determining difference in the codes modulated onto the signal. In phase based measurement, such as the experiment done by Liu et al. [2017], ranges can also be found by resolving for the phase ambiguity. The phase based approach is in general more accurate, but is significantly more time-consuming. In addition, the Doppler-effect is considered, as a change in observed frequency will necessarily change the observed range unless it is taken into account.

The main product created from the reflectometry method is what is known as a *Delay Doppler Map* (DDM). This is a grid which represents all correlation responses as a function of time delay and Doppler shift, where each cell is computed using the method described in 2.3.1. Figure 10 Shows an example of a DDM created using UK-DMC-1 data. We can observe that the response is very varied, but with clear peaks. The largest peak can be identified as the response of the direct signal. The characteristics of the expected responses in a DDM varies with which type of observation we are making. For a ground based experiment, the expected timing differences between the direct and reflected signal is small seeing as the receiver will be close to the reflecting surface, resulting in a short range difference. The code delay component of the DDM will therefore be very close to the response of the direct signal. By observing both the code delay and the Doppler

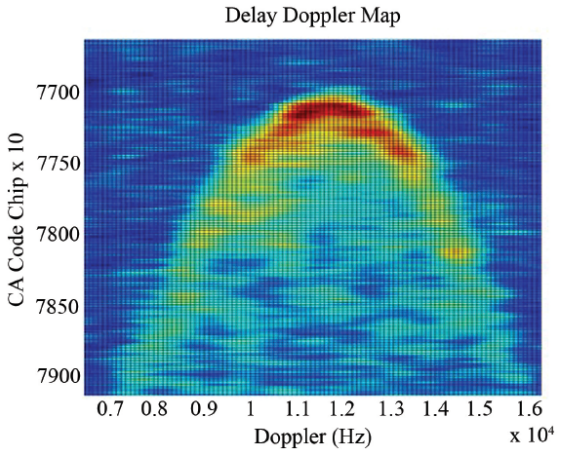

Figure 10: An example of a Delay Doppler Map as presented by Ruf et al. [2016]. The more a value tends towards red, the stronger the response.

frequency, it is possible to compute the range difference $\Delta\rho$ of the specular points reflected off the surface. Furthermore, Liu et al. [2017] Gave the following relation between the range difference and the surface height:

$$\Delta\rho = 2h \cdot sin(el) + \vec{e} \cdot \vec{b} \tag{12}$$

where h is the height difference between the surface and the downwards looking antenna, el is the elevation angle, $\vec{e}$ ia the unit vector pointing in the direction of the directly received signal for the upwards looking antenna, and $\vec{b}$ is the base between the upwards and downwards looking antennas. Figure 11 shows the concept of Equation 12. When detemining the height however,

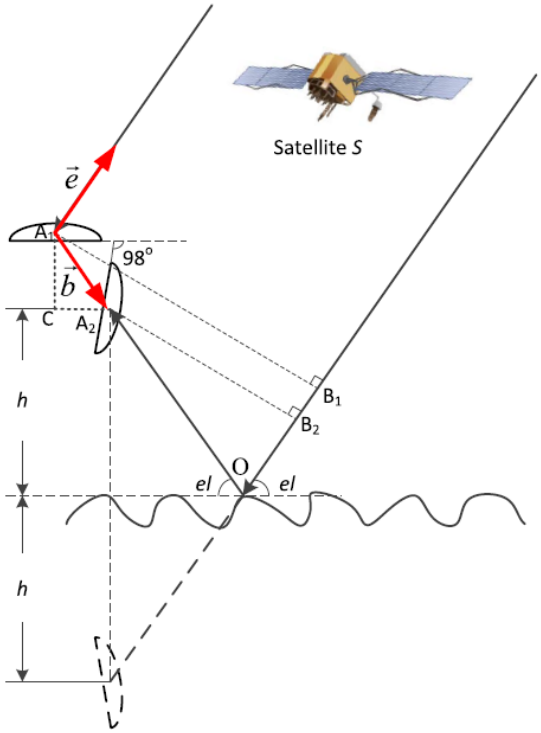

Figure 11: The principle of height determination as presented by Liu et al. [2017].

we do not observe the range differences directly. As will be further discussed in Section 4.2, we observe the period of the interferometric pattern created by the correlation of the direct and reflected signals. This quantity can be

expressed as $d\rho/(dt\lambda)$. We therefore get

$$f_{int} = 1/T_{int} = \frac{d\rho/dt}{\lambda} = \frac{2h \cdot cos(el)de/dt}{\lambda} \tag{13}$$

where f is the frequency of the interferometric pattern, T is the period and λ is the carrier wavelength of the original signal. By rearranging the terms we can get an equation to determine the height:

$$h = \frac{\lambda dt}{2f_{int}cos(el)de} \tag{14}$$

The Normalized Bistatic Radas Cross Section (*NBRCS* or *BRCS*) is also an essential parameter in reflectometry. As mentioned in Section 2.3.1, the BCRS is an important parameter for describing the size of the glistening zone. It can be viewed as the ability of a surface to reflect the signal of a radar signal [Toomay, 1989]. In our case, the signals considered are GPS signals. Equation 8 describes the observed power for a given code delay and freqency shift as a function dependent on the BCRS. It is therefore important to be able to determine it precisely. Ruf et al. [2016] define the BCRS as:

$$\sigma_0 = \pi|\Re|(q/q_z)^4 P(-q_\perp/q_z) \tag{15}$$

where $|\Re|$ is the complex Fresnel coefficient, q is the scattering vector, which is dependent on the coordinate of the reflecting point. $P(\vec{s})$ is the probability density function (PDF) of large scale slopes. The reason why the PDF only considers large scale slopes is due to the limits of the Kirchhoff approximation, as it considers all contributions as a sum of contributions from "well behaved facets". As these facets have to be large enough for the reflections to be present, smaller variations have to be ignored. The PDF is defined as:

$$P(\vec{s}) = \frac{1}{2\pi\sqrt{mss_x mss_y(1-b_{x,y}^2)}} exp\left[-\frac{1}{2(1-b_{x,y}^2}(\frac{s_x^2}{mss_x} - 2b_{x,y}\frac{s_x s_y}{\sqrt{mss_x mss_y}} + \frac{s_y^2}{mss_y})\right] \tag{16}$$

where $b_{x,y}$ is the correlation coefficient between the slope components. mss_x and mss_y are the *Mean Square Slope* in the along and across wind direction respectively. The Mean Square Slope (MSS) is a metric for describing the

surface roughness, where a larger MSS implies that the sea surface is rougher, which will lead to a more diffuse behavior in the scattering. Additionally, the orthogonal components of the MSS shows that our observations will be dependent on both the wind speed and direction. If we combine Equation 15 and 16, we can observe that the BRCS, and therefore the ability of the surface to reflect the signal, is dependent on the state of the ocean. This follows the intuition from previously as the PDF has smaller tails when the MSS has a low value. This implies a lower MSS will yield a stronger specular reflection.

Semmling et al. [2019] defined the Fresnel reflection coefficient through a set of equations. Firstly, they made a distinction between the co-polar and cross-polar (in-phase and quadrature) Fresnel coefficients:

$$\Re^{co} = \frac{1}{2}(\Re_{\parallel} + \Re_{\perp}) \tag{17}$$

$$\Re^{cross} = \frac{1}{2}(\Re_{\parallel} - \Re_{\perp}) \tag{18}$$

where $\Re_{\parallel}$ and $\Re_{\perp}$ are the components parallel and perpendicular to the incidence plane respectively, defined as:

$$\Re_{\parallel} = \frac{\epsilon_{sea} sin\Theta - \sqrt{\epsilon_{air}\epsilon_{sea} - (\epsilon_{air} cos\Theta)^2}}{\epsilon_{sea} sin\Theta + \sqrt{\epsilon_{air}\epsilon_{sea} - (\epsilon_{air} cos\Theta)^2}} \tag{19}$$

$$\Re_{\perp} = \frac{\epsilon_{air} sin\Theta - \sqrt{\epsilon_{air}\epsilon_{sea} - (\epsilon_{air} cos\Theta)^2}}{\epsilon_{air} sin\Theta + \sqrt{\epsilon_{air}\epsilon_{sea} - (\epsilon_{air} cos\Theta)^2}} \tag{20}$$

ϵ_x is the permittivity of medium x, and Θ is the elevation angle of the reflected signal. The fact that $\Re$ is highly dependent on the permittivities of the traversing medium and the reflecting medium is intuitive as it is correlated with the refractive indices of the media [Cooper, 2013]. When a signal encounters a new medium with a different permittivity, the signal is affected as some parts of the signal will be reflected off the surface, while other parts of the signal will be refracted in the second medium, as shown in Figure 12.

2.4.1 Parameters Affecting the Observables

Similarly to common GNSS measurements, several different factors affect the signal. It is detrimental that we manage to model these factors, as ignoring

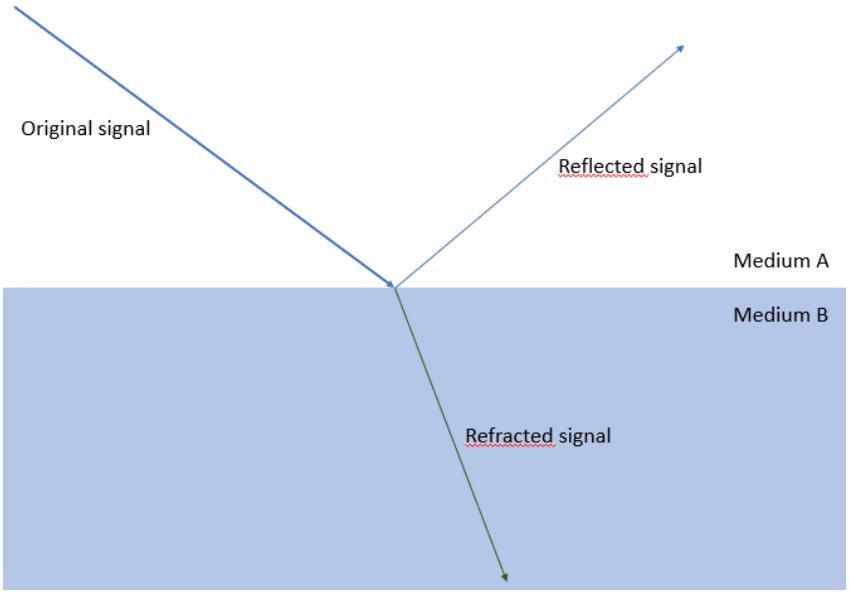

Figure 12: Signal going through different media. The difference in permittivities causes the signal to partly reflect off the line between med media, and partly refract into the new medium.

these factors will cause our observations to contain large errors. Liu et al. [2017] provided a formula for explaining how the observed phase got created. It was defined as:

$$\Delta\phi = \Delta\rho + \delta_{TROP} - \delta_{IONO} + \delta_{APC} + \delta_{PWU} + \lambda N + \epsilon \tag{21}$$

where $\Delta\rho$ is the path delay for the reflected signal with respect to the direct signal, δ_{TROP} and δ_{IONO} are the delays caused by the signal travelling through the troposphere and ionosphere respectively. For airborne and space borne missions, these differences can be substantial as the reflected signal has to travel through these atmospheric layers for a significantly longer distance. The author does however argue that for a ground based experiment the differences will be negligible. δ_{APC} is the difference in the phase center variation (PCV) between the direct and reflected signals. δ_{PWU} is the difference in the phase wind-up effect between the direct and reflected signal. Both δ_{APC} and δ_{PWU} are dependent on the elevation and azimuth angle of the satellite. N is the phase ambiguity. This number tells the difference in completed cycles of the carrier phase, similar to normal GNSS phase measurements, and yields much more accurate range measurements compared to code pseudorange if the ambiguity can be solved for. ϵ is the remaining errors not modelled by Equation 21.

The phase wind-up effect is an error introduced by a change in the orientation between the satellite and the receiver [Beyerle, 2008]. This orientation varies with time due to the movement of the satellites and its change in orientation to focus the signal towards the Earth centre of mass. When the orientation change, this induces a shift in the observed signal. If not taken into account, this shift can mistakenly be seen as a range difference. Liu et al. [2017] compared the effect of the phase wind-up for the directly received signal and the reflected signal and found that this difference can be several centimeters. For certain applications, such as altimetry, such a large error cannot be tolerated if the GNSS-R method is to be considered viable. They therefore consider the correction

$$\delta_{PWU} = \Delta\phi^{refl} - \Delta\phi^{dire} \tag{22}$$

where

$$\Delta\phi^{refl/dire} = \phi^{refl/dire}_{LHCP} - \phi^{refl/dire}_{RHCP} \tag{23}$$

ϕ notes the phase caused by the wind-up effect, *refl/dire* means reflected or direct signal and RHCP/LHCP notes the polarization of the considered wave. Beyerle [2008] derived the contributions of these components

Phase center variations are caused by the fact that the phase center is not perfectly aligned with the geometric center of the antenna [Subirana et al., 2011]. Furthermore, these offsets are dependent on the frequency of the signal as well as the previously mentioned elevation and azimuth angles. These offsets are also different for the different polarizations. Liu et al. [2017] therefore express the difference in phase center variation as:

$$\delta_{APC} = \delta_{PCC}^{LHCP} - \delta_{PCC}^{RHCP} \tag{24}$$

where $\delta_{PCC}^{LHCP/RHCP}$ is the phase center corrections for the left handed and right handed signals. The phase center corrections are much smaller compared to the phase wind-up effect, being around a $1cm$ at max.

3 Instrumentation and Data Handling

This section describes the setup used for a ground-based GNSS-R experiment. The data collected from this station is used for the reflectometric measurements. First, the antenna setup, which is similar to the setup used by Liu et al. [2017], will be presented. Next, a brief introduction to the GNSS-R receiver used in this experiment is given. Lastly, the parsing of the data received from the receiver will be explained.

3.1 Experiment setup

The data used in the experiment was retrieved from a receiver mounted in Onsala, Sweden. The setup was used by Liu et al. [2017] for phase altimetry. Figure 13 shows the setup. The setup consists of a GNSS-R receiver, which

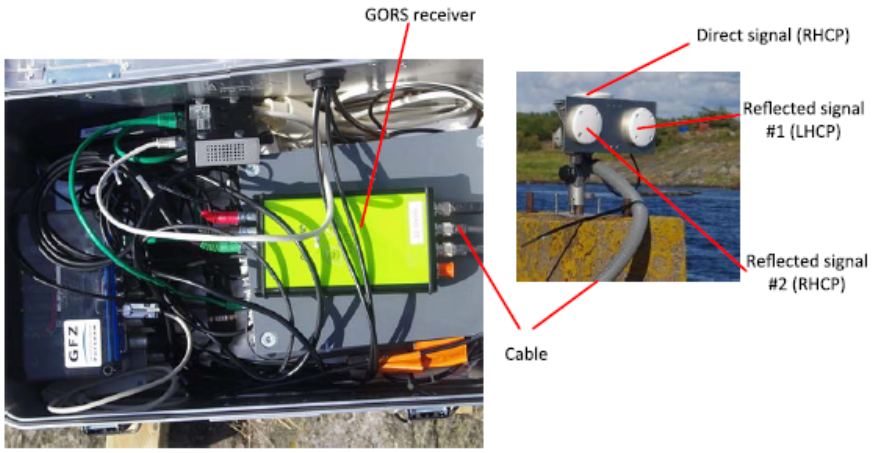

Figure 13: Setup of the experiment at Onsala, courtesy of Liu et al. [2017]. The antenna aimed at receiving the direct signal is aimed upwards and receives right handed signals, while the tilted antennas are aimed at reflections. There is both a right handed and a left handed tilted antenna.

is described in Section 3.3, along with 3 antennas: One looking in the zenith direction used for tracking the direct signals, and two being tilted towards the sea used to track reflection events. One of the side-looking antennas has RHCP polarization to detect the right handed reflected signals, while the other with LHCP polarization is configured for the left handed reflected signals. Additionally, the side looking antennas is considered to have a cutoff azimuth angle in the range $75^o - 220^o$. This is done to avoid multipath contributions from nearby irrelevant surfaces. The antennas were mounted at approximately $3m$ above sea level. The experiment is described in more detail by Liu et al. [2017].

3.2 Antennae specification

The antennas used in the experiment are the AntCom 3G1215 model. The two side-looking antenna support dual-polarization observations. It is therefore capable of capturing both left and right handed reflections. Palamartchouk et al. [2015] used these antennas in their research on multipath mitigation and presented the gain patterns of the antenna, which can be found in Figure 14.

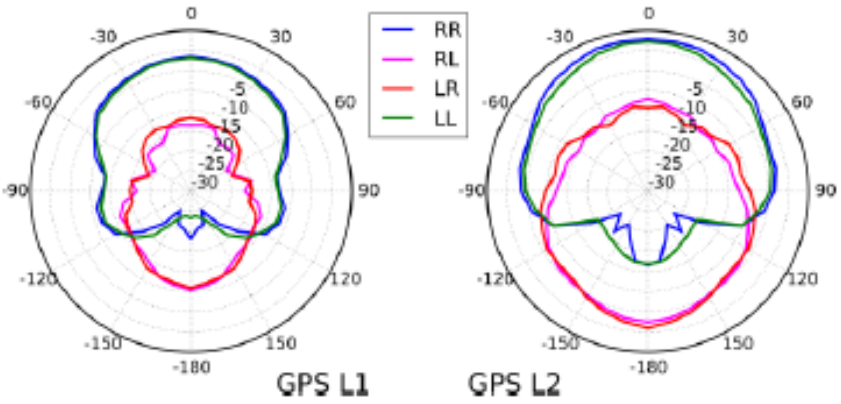

Figure 14: Documented gain patterns for the AntCom 3G1215RL antenna, originally presented by Palamartchouk et al. [2015]

Using a dual-polarization antenna is beneficial for the experiment as each reflected change the polarization of the signal [Nievinski and Larson, 2014].

This is because over different elevation angles the co-polarization (RHCP) or cross-polarization (LHCP) reflections account for parts of the overall reflection event.For instance over higher elevation angles we expect a larger contribution of left handed reflections coming from the surface while over grazing angles the right-handed part play a significant role. In the experiment performed by Palamartchouk et al. [2015] the tracking of indirect signals is much more difficult due to large variability in surrounding geometry, the loss of power caused by the reflecting surface and the degradation of the SNR in reflected signals.

As we can observe, the gain is non-zero for its unintended configuration (LR and RL), and can even be the dominant component for angles below the horizon. The experiment at Onsala, which can be found in Figure 13, tilts the antennas towards the sea. By doing this, the received signals will to a larger degree pass through the antenna in its highest gain region.

We can also observe that the gain patterns are different for the carriers ($L1$ and $L2$). This is to be expected as the carriers are transmitted with different power from the GPS satellites.

3.3 Reflectometry Receiver

The receiver used in the experiment is the GNSS occultation, reflectometry and scatterometry (GORS) receiver developed and manufactured by JAVAD. This receiver is specialized for reflectometry, scatterometry and occulation purposes. It performs the all of the traditional front-end tasks, as described in Section 2.2.2. Furthermore, it performs the necessary correlation tasks, which are described in Section 2.2.3. The receiver has one *master channel*, which is responsible for tracking the direct signal, and three *slave channels* used for recording reflections. Figure 15 illustrate the relation between the antennas and the channels. We observe that the slave channels depend on data from the master channel. This is to be expected as we need delay and Doppler information from the direct signal to make reflectometry measurements and infer properties of the reflecting surface, as described in Section 2.2.3.

The main output of the receiver is the in-phase (I) and quadrature (Q) correlation sums as well as standard messages from the the tracked direct signal. The frequency of the I/Q outputs is one sample every 5ms, or 200Hz.

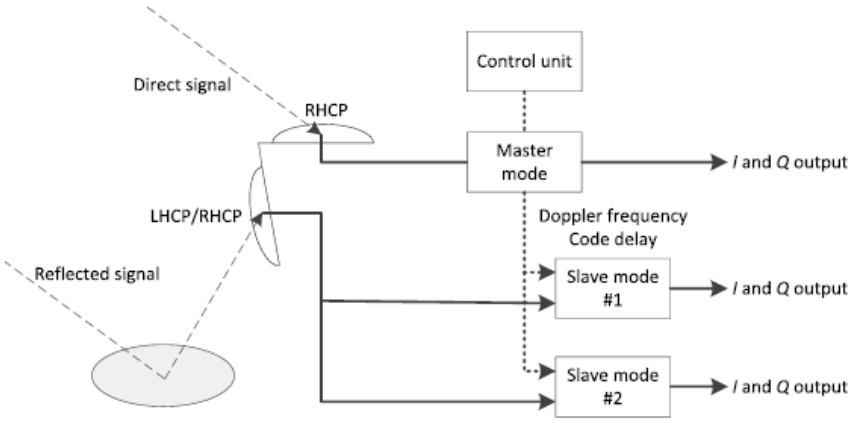

Figure 15: Schematic of a GORS receiver, courtesy Liu et al. [2017]. Both the master and the slave correlators output I and Q correlation data.

3.4 Handling Data Stream

The data recorded by the receiver is fed to a Python script as a byte stream. The script is responsible for parsing this stream and save any messages of interest to a structure for later analysis. The Python script receives the message over TCP. In the case of the Onsala data, the data is streamed through a local TCP socket as this data is not recorded in real-time, but is saved as a pre-formatted file. We use a test receiver at the department of civil and environmental engineering (IBM), NTNU, to check the performance of the data handling software. For the receiver at NTNU, the software connects to one of the five available TCP connections of the receiver which are dedicated to sending and receiving data streams and instructing the receiver. This enables the software to both send commands to the receiver and receive the data through the same port.

During the reflectometry measurements, it is of interest to be able to extract and estimate geophysical parameters as data is received. Real-time processing of data would be beneficial for certain applications, such as real time monitoring of sea surface roughness and sea surface height. However, the real-time aspect also introduces some requirements and challenges for the software. Firstly, several computations has to be done in real time. It is therefore important that these computations do not create a bottleneck in the software. There is a risk of creating such a bottleneck as each message

to be parsed will be validated by a checksum. As we are parsing several thousands of lines each second, it is detrimental that these computations are performed at a sufficient speed.

Secondly, it is important that the parser correctly manages to identify messages of interest, and rejects both messages which are irrelevant or are erroneous. As previously mentioned, each message contains a checksum which we can compute from the byte sequence. Additionally, each message is terminated by a *newline byte*. This byte value is however not exclusive for message separators. When encountering this byte value, it is therefore important to correctly decide whether it terminates a message or not. If not, it would invalidate the message as the checksum would be incorrect.

One final consideration which has to be addressed when reading the data, is that we may stop reading in the middle of a message. In Python sockets, we have to specify the number of bytes we read, and then read the data in chunks of the specified size. We therefore have no guarantee that a message is complete when a chunk is done. Additionally, we cannot necessarily guarantee that the start of a chunk will be the start of a message. We therefore have to check whether the previously processed line was incomplete. Additionally, we have to know if the previous termination was caused by a newline in the byte stream or not.

Figure 16 shows a flowchart of the Python implementation. The script starts by listening for a byte stream on the server it has connected to. When a line is received, it goes through a set of checks to determine how to process it further. In the case of an empty byte array, the script closes its connection, saves the data to a file and terminates. If this is not the case, the line is further evaluated. Each new line of data should be prefixed by a header containing a message identifier and the size of the message. The message identifier is always alphanumerical, except for specific time headers which are accounted for. In other words, if the first two characters in the byte stream are not alphanumerical, we are not currently at the start of a new message. The script will then try to prepend the previously stored line to the line. Whether the previous line is stored or not is dependent on whether it has the correct length which is stated in the header. If it is too short, it will store it for the next line. If it is too long, it will proceed and invalidate the line.

If the header is alphanumerical and is of the correct length, the script further determines which specific header it is and how to process it. If it is not in the set of headers found in Table 1, the line is ignored, and the next

line is processed.

Table 1: Headers considered by the script. Header definitions taken from the GREIS documentation [GNSS, 2020]

Header	**Explanation**
Ix	In-phase correlation output from channel x
Qx	Quadrature correlation output from channel x
~~	Receiver time. Defined as the time of the current day
RT	Same as ~~
::	Epoch time. This value defines the end of the epoch, where ~~would signal the start of one
GT	GPS time. Defined by the GPS week and the time of week (ms)
RD	Receiver date. contains the year, month and day of the receiver clock.
AN	Antenna names. Enables identification of which antenna a message is coming from.
SI	Satellite identity. contains a list of Universal Satellite Identities (USI) of all satellites in sight.
SX	Same as SI, but only used in later versions. All newer implementations are however backwards compatible with SI.
EL	A list of all elevation angles of the satellites in sight
AZ	A list of all azimuth angles of the satellites in sight

Headers with identifier Ix or Qx are in-phase and quadrature correlation output of channel x. The master channel previously described, which can be seen in Figure 15 is identified using channel C. Each channel has its own time-series which is stored for later analysis. Each channel also has separate time series for each satellite, which can be identified by a satellite id found in the message.

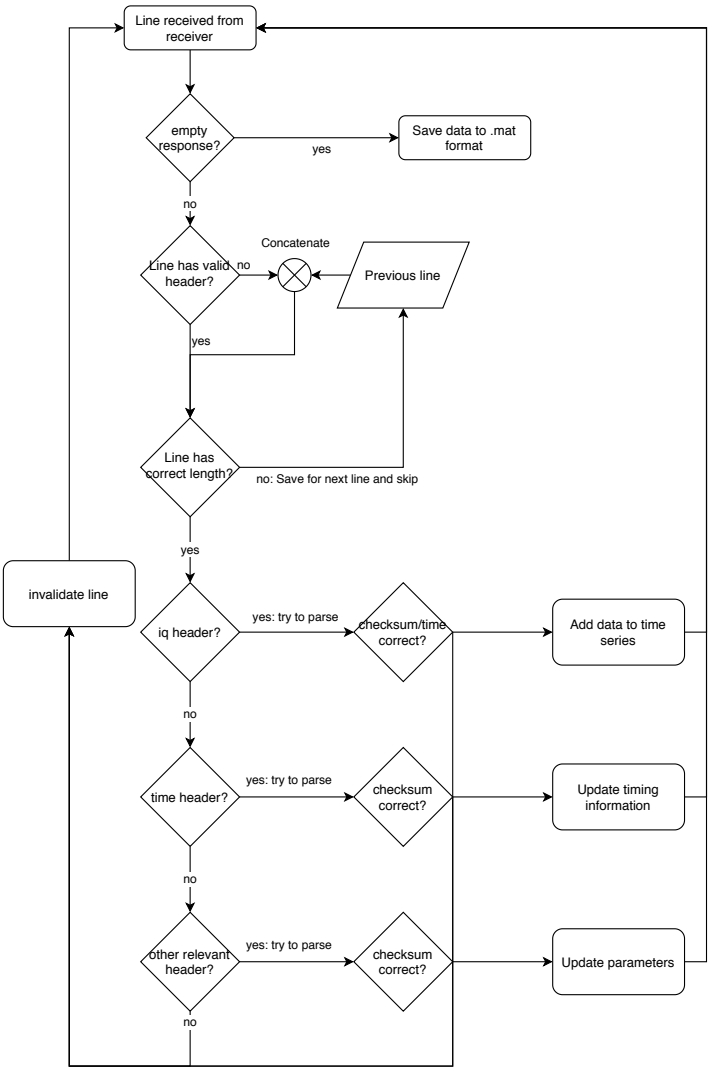

Figure 16: Flowchart of data stream handler

4 Dataset and method

This section introduces the datasets used in the thesis. The datsets include both the data received from the GORS receiver and the ancillary data used for verification of results. Additionally, the methodology of processing the data is described here.

4.1 Main dataset

The data used for the extraction of geophysical parameters is retrieved from the station set up at Onsala by Liu et al. [2017]. The data is served as a byte stream where each message follows the GREIS documentation specification [GNSS, 2020]. The time span of the data used in this study is from 09.05.2020 to 12.05.2020.

To verify the processing results of reflectometric observations, we use an ancillary dataset released by the Swedish Meteorological and Hydrological Institute (SMHI). Different observations have been made publicly available online through the SMHI website, one of which is tide gauge data with a temporal resolution of one minute from a set of measurement stations in Sweden. The data can be found at `https://www.smhi.se/en`. We use the tide gauge measurements from a station located at Onsala close to the setup of the reflectometry experiment. The two observation sites, i.e. the tide gauge station and GNSS-R setup, are separated by a direct distance of about 340m.

Finally, the wind speed at the time of measurement will be used to investigate how both the wind speed and its direction can affect our observations. This data is also retrieved from SMHI, and is released with an hourly resolution.

4.2 Data analysis

To be able to perform altimetry, we need a relation between the correlation output from the GORS receiver and the height of the reflecting surface, i.e. sea water. Equation 12 provides us with a relation between the observed range differences as a function of elevation angle and height. The elevation

angle is known from the broadcast ephemeris, while the height and range difference remains to be determined. If we rather use the derivative with respect to the time, Equation 14, we can express the frequency as a function of antenna height with respect to the reflecting surface and elevation angle. The frequency or its reciprocal form the period, while not known exactly, can be observed from the correlation output. Two methods used for finding and extracting this period will be further described in the next section. The methods are the *Singular Spectrum Analysis* (SSA) and *Wavelet* analysis.

4.2.1 Singular Spectrum Analysis

The *Singular Spectrum Analsysis*, or SSA, is a non-parametric estimation method used for extracting information from data with a lot of noise [Stephenson, 2009]. It therefore does not make any assumptions regarding the data unlike many other estimation methods. As explained by Golyandina and Zhigljavsky [2013], the method consists of several steps which enables feature extraction. One of the most common application of the SSA method is the trend extraction. The SSA performs the following step to retrieve a trend representation of a time series.

The first step in SSA is to create a set of *lagged vectors* from the original time series. This is achieved by using a sliding window approach with a window of constant size. The window moves along the time series and captures the elements inside the window. These entries are then inserted into the columns of a matrix which is used for further processing. Given a time series of length X, and a window of length N, the final matrix of lagged vectors, referred to as the *trajectory matrix* in literature, will be of the dimension $N \times (X - N + 1)$.

After the trajectory matrix is created, we can identify several features of the function which characterize the time series. This is achieved through *Principal Component analysis* (PCA). The PCA applies Singular Value Decomposition (SVD) to the trajectory matrix to create a set of orthogonal basis functions. The SVD decomposes the trajectory matrix as $X = U\Sigma V^T$ where Σ is a rectangular diagonal matrix while U and V are orthogonal matrices. The diagonal elements of Σ can be computed as the square root of the eigenvalues of XX^T or X^TX. The SVD representation of X can be formulated as

$$X_i = \sqrt{\lambda_i} U_i V_i^T, i \in (1, rank(\Sigma)) \tag{25}$$

Here, λ_i is an eigenvalue of XX^T, and U_i, V_i are the eigenvectors associated

with the eigenvalue, derived from XX^T and X^TX respectively. The eigenvalues are ordered such that $\lambda_i \geq \lambda_{i+1}$. All X_i are full rank and describe parts of the variability in the function through some feature, where we expect earlier X_i to represent a greater part of the variability. The SVD representation of X is therefore the sum of all X_i, up to the rank of X. From this definition, we can define a set of *Eigentriples* which contain $(\sqrt{\lambda_i}, U_i, V_i)$.

After the SVD representation is created, we continue by grouping all of the eigentriples into disjoint sets. The choice of which elements to select is determined by what part of the variability we are aiming to model. The high frequency variation in the dataset would be usually expressed in the eigentriples with low eigenvalues. The general trends of the time series, could be retrieved by eigentriples with large eigenvalues [Hoseini et al., 2019].

After the proper set has been selected, we proceed with the final step of the SSA algorithm, which is the diagonal averaging. The goal of this step is to recreate the time series given the new set of X_i chosen to represent the trajectory matrix of the function. In the original trajectory matrix, we can easily identify similar elements on the anti-diagonals as each consecutive row is delayed compared to the previous one. In the reconstructed matrix however, this is not the case. This motivates the necessity for the diagonal averaging, as we replace the elements of the anti-diagonals with an average value of all of the its elements. After this is done, we can obtain the reconstructed series by inverting the first step of the algorithm.

Figure 17 shows a comparison of the input data, which contains a lot of high frequency noise, and the output data of the SSA.

4.2.2 Wavelet

Wavelet analysis is a method to examine the presence of different frequency components in a function. The wavelet functions are similar to Fourier representations, except the function is localized in time, meaning the function is zero at all points except for the intended area (similar to a Dirac delta function). The area under the curve of a wavelet is always zero. In wavelet analysis, the data to be analysed is compared to a reference wavelet, or an *analysing wavelet*. Several different wavelets are often used, such as the one in Figure 18.

When performing wavelet analysis, we cross correlate the relevant data with the analysing wavelet. The wavelet analysis produces a 2-dimensional search space as we vary translation and scale. By translation, we refer to

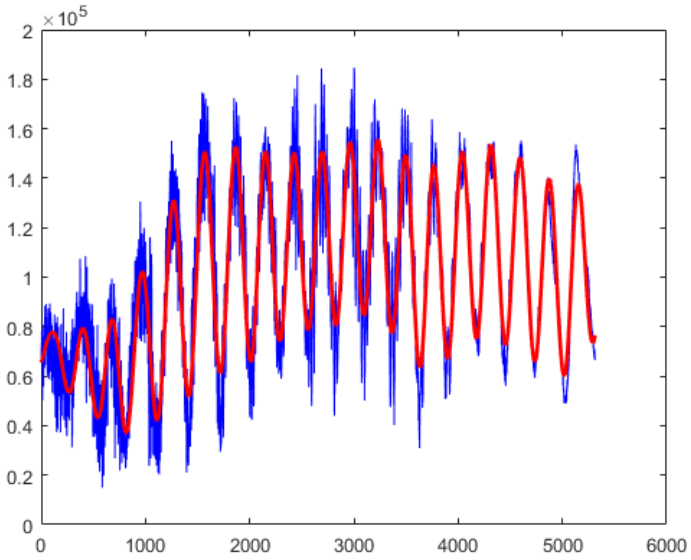

Figure 17: Figure showing the output of the SSA algorithm (red) given noisy input (blue)

the act of moving the analysing wavelet along the dataset to produce a correlation for the entire function. By scaling we refer to changing the period of the analysing wavelet by "stretching" or "squashing" it. Figure 19 shows an example of how the search space may look. By looking for maxima in this search-space, we can identify subsets of data which exhibit the periodic behavior described by the analysing wavelet.

In addition to be looking for global maximas, we may only be interested in areas which contain specific periods. For the Onsala receiver, the receiver is around 3m above sea level [Liu et al., 2017]. Based on Equation 14 and our desired interval of variables, we can reduce the search space significantly. Figure 20 Show the same wavelet responses, but with the periods considered only going from $190s - 640s$.

4.2.3 Evaluation of Errors

Equation 14 provides us with an opportunity to estimate the height from the elevation angles and the period observed from the wavelet analysis. However, the observed values contain uncertainty which has to be considered as the

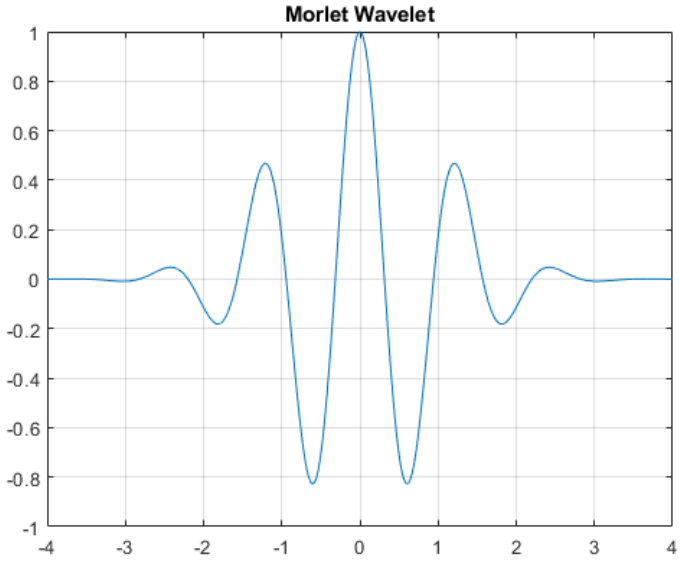

Figure 18: The Morlet wavelet, as presented in the MATLAB documentation

errors in our observables will propagate to the final height. In general, given a function $f(x_1, x_2, ..., x_n)$ where each variable has an error of ϵ_i, we can formulate the upper-band error of f as:

$$\epsilon^2 = \sum_{i=1}^{n} \left(\frac{\partial f}{\partial x_i} \right)^2 \cdot \epsilon_i^2 \tag{26}$$

Equation 14 expresses the height as a function of elevation angle, elevation angle rate and observed period. We therefore get the the following expression for the error in our observed heights:

$$\epsilon^2 = \left(\frac{\lambda}{2T^2 cos(e) e'} \right)^2 \epsilon_T^2 + \left(\frac{\lambda tan(e)}{2T cos(e) e'} \right)^2 \epsilon_e^2 + \left(\frac{\lambda}{2T cos(e) e'^2} \right)^2 \epsilon_{e'}^2 \tag{27}$$

where λ is the carrier wavelength, T is the period retrieved from the wavelet analysis, e is the elevation angle read from the data stream, and e' is the change in the elevation angle, calculated from the observed elevation angles.

To determine the scale of the values of ϵ_e and $\epsilon_{e'}$, a separate set of data is used which provide both the values broadcast by the satellties themselves as well as the precise ephemeris which are produced by International GNSS

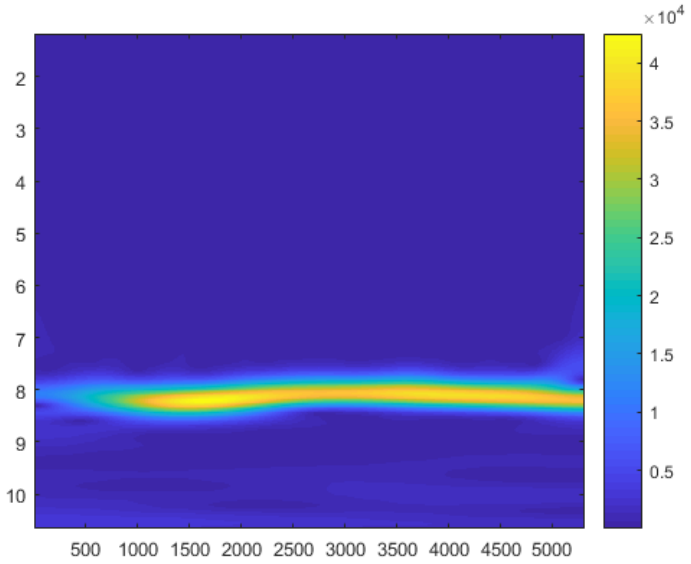

Figure 19: Example of wavelet responses over the 2D search space. The x-axis represents the translation of the wavelet, while the y-axis represent the logarithm of the period used by the analysing wavelet.

Service (IGS) processing center. ϵ_T can be determined by the resolution of the wavelet analysis, as we represent a set of discrete periods. The step size between the periods determine how large the error in the period can be and will be used for error estimations.

4.3 Data Processing

From the script of reading the raw data files in python, which is described in Section 3.4, we have several datasets containing essential information for performing altimetry. The datasets include the elevation angles and azimuth angles of the tracked satellites as well as the correlation sums of the I/Q channels. We use a 1-Hz time resolution for the I/Q sample time series. These time series are then aligned. If we are unable to locate an elevation angle, an azimuth angle and at least one correlation output for a given epoch, all data associated with this epoch is discarded as it cannot be used for our measurements.

In Section 2.4 we discussed the importance of having the conditions re-

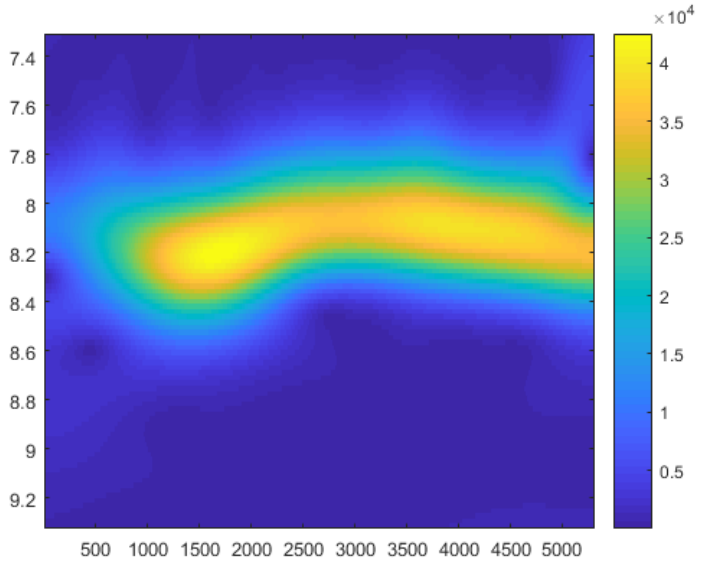

Figure 20: The wavelet search space reduced to the area of interest

quired to perform reflectometry measurements. Equation 19 and 20 describe the impact of the elevation angle for the strength of reflected signal considering the permittivity of the reflecting media. Besides, the roughness of the reflecting surface also affects the reflection power. Reflections coming from the grazing angles will have a larger portion of its signal reflected off the surface. To take these factors into account, observations in the interval $[3, 40]$ degrees are considered for the altimetry, while others are discarded.

The elevation angles obtained from the receiver messages are very coarse and contain significant uncertainties. As a result, they are provided with a step size of 1 degree. For computations, the elevation angles are interpolated to fit these value jumps. This process also checks the magnitude of the jumps in data, as we do not expect the elevation angle to have large jumps. Data entries with such jumps are discarded.

From the aligned time series, we are able to observe its period which will further be used for height determination. To find this period the methods described in Section 4.2. First, the SSA algorithm is applied to the correlation output. The selection of the eigentriples in the reconstruction step enables us to think of the method as a low-pass filter which eliminates high-frequency noise from the data. Figure 17 illustrates this, where the SSA output largely

reflects the long-term, low frequency trends of the input data. This time series is then analysed using the Morse wavelet. Based on the height of the sea surface (3 m) from the installation of the antennas, we will consider a selected interval of the periods, i.e. $[190, 640]s$. The observed period for a given time period is then chosen as the maximum power response of the wavelet analysis at a given epoch. Figure 21 shows the period extracted from Figure 20.

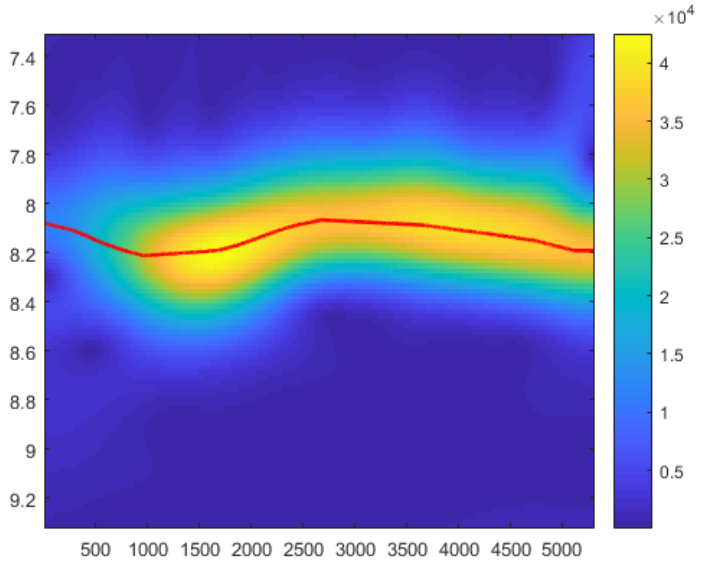

Figure 21: The observed function retrieved from the wavelet analysis

When the period is extracted, we have all the necessary components to compute the heights from Equation 14.

An estimation of the location of the specular point is then computed for each height together with the information of elevation and azimuth angles. This can be used to filter out the specular points over the land. As the specular point is the center of the glistening zone, it serves as a simple method of rejecting out of bounds reflections. The distances dx, dy of the specular point from the receiver can be computed as:

$$[dx, dy] = \frac{h}{tan(el)}[sin(az), cos(az)] \tag{28}$$

where h is the computed height, el is the elevation angle and az is the azimuth angle. The coordinate of the specular point can then be computed as

$$[B, L] = [B_0, L_0] + [dy, dx]\frac{180}{\pi R} \tag{29}$$

where B_0, L_0 is the latitude and longitude of the receiver and R is the radius of the Earth.

A weight is also assigned to each height observation. From Figure 21 we can observe that the observed power for the chosen period varies over time. The strength of reflection in the time series makes the height retrieval easier and more reliable. Therefore, the reflection power will be used for the weight of the observations. We would also have several satellites in view at each epoch which could be used for height computations. Each of the the incoming direct signals from differnt satellites might have different powers. To take this aspect into account, the ratio of observed power to the power of the direct signal is used for the weighting. To use this ratio, the received powers have to be corrected for the gain of the antenna based on the direction of reception (Figure 14).

Additionally, we have previously observed that observations at lower elevation angles should reflect larger parts of the signal towards the receiver. Elevation angles closer to the horizon should therefore have larger weights.

To reflect the aspects described above, the weights of the observations were chosen to be

$$w_i = p_i cos^2(e_i) \tag{30}$$

where w_i is the weight at time i, p_i is the gain corrected power ratio between the reflected and the direct signal at time i and e_i is the elevation angle at time i.

For our final height estimation, the weighted average of the height estimations are used. Rather than computing an absolute height for each epoch, the height anomaly is computed. The height anomaly is computed by observing change in height from some time t_0. This is done as we are interested in observing the changes in the measured heights rather than the heights themselves. The height anomalies are aggregated from 1 second values to 1 minute values, with t_0 set to the first entry in the subset used in the aggregation. In this aggregation process jumps in data are also rejected if the change in height is unreasonable. A sudden jump in height of for example $50cm$ would be ignored as we do not expect the sea level to change by this amount over such a short time span.

5 Results and Discussion

In this section, the results of the data analysis will be presented and discussed. The computed heights will first be presented and discussed. Afterwards, the height anomalies are computed and compared to tide gauge data. Finally, the errors and the impact of errors in our observations will be discussed.

5.1 Height Observations

Heights were estimated using Equation 14 for 5 different time intervals, each spanning between 2-4 hours. Figure 22 Shows the heights computed on 05.09.2020 along with the upper bands of the errors estimated from Equation 27. By comparing the estimates using the broadcast orbit information and the precise orbit data released by IGS, the values chosen for ϵ_e and $\epsilon_{e'}$ were 1 degree and $1e-5rad/s$ respectively. The observed averages and standard deviations of the elevation angle and its rate of change can be found in Table 2. The variable ϵ_T was set to 5 seconds as this was the step size of consecutive periods around 300 seconds.

Table 2: Absolute differences between precise orbit information and the broadcast ephemeris

-	average	σ
e	0.30 degrees	0.1475 degrees
de	9.26e-6 rad/s	2.2681e-6 rad/s

From Figure 22, we can observe that several of the satellites are within the error estimates of each other. However, we can also observe that this is not always the case as for example PRN 12 are around 1 meter above the other satellites.

Figure 23 show the specular points estimated using Equation 29 for the heights found in Figure 22. As we can observe, the specular points for PRN 18, 21, 29 are very close to the coastline, while the remaining satellites have longer tracks of reflections. Furthermore, the specular points close to the

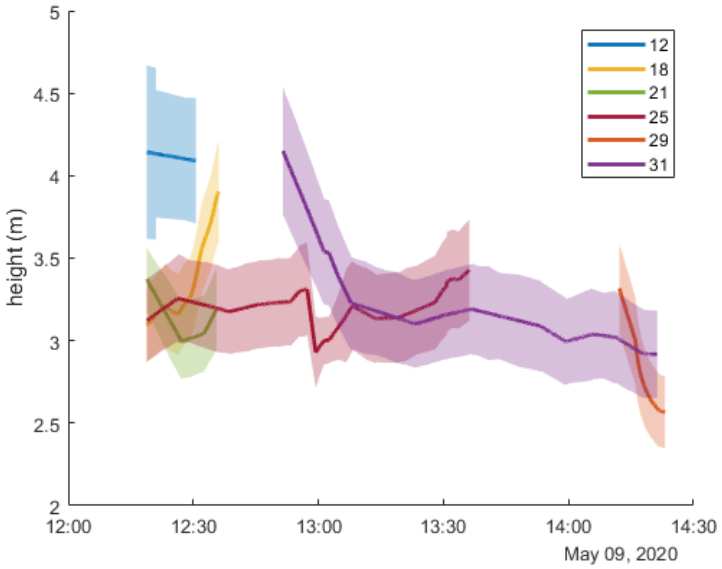

Figure 22: Heights estimated from cross-polar signal reflected off the ocean surface on 09.05.2020. The shaded area represent the estimated errors of the observations.

coastline are associated with larger elevation angles. As previously discussed, this implies that we expect less of the signal power to be reflected off the surface. Thus, we expect the observations from these satellites to express larger variation. Additionally, Figure 24 shows that there is a greater variability observed for observations close to the coastline. This may imply that this data should be filtered out to reduce this error.

It can be observed that the gradient of PRN 18 and 29 seem to be vastly different compared to the trends of the other satellites. Furthermore, we can observe that there are several time periods in which few satellites are visible, which reduces the redundancy of final height anomaly estimations. Figure 25 show that we sometimes lack usable satellites for reflectometry.

It is important to consider the validity of the computed heights. Figure 26 show the heights computed on 10.05.2020. The behavior of the computed heights from PRN 10 and 20 differ significantly compared to the other ones. The value of the heights are vastly larger compared to the other satellites. A cause of this error could be related to the lack of weaker reflection powers. Also of note is the large observed errors in elevation angle values. The loca-

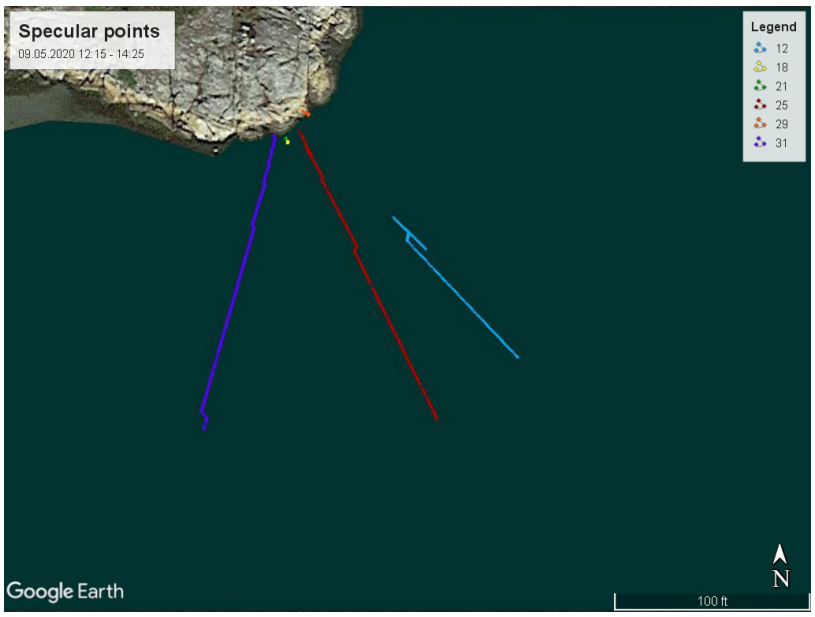

Figure 23: Specular points for the different satellites used in Figure 22

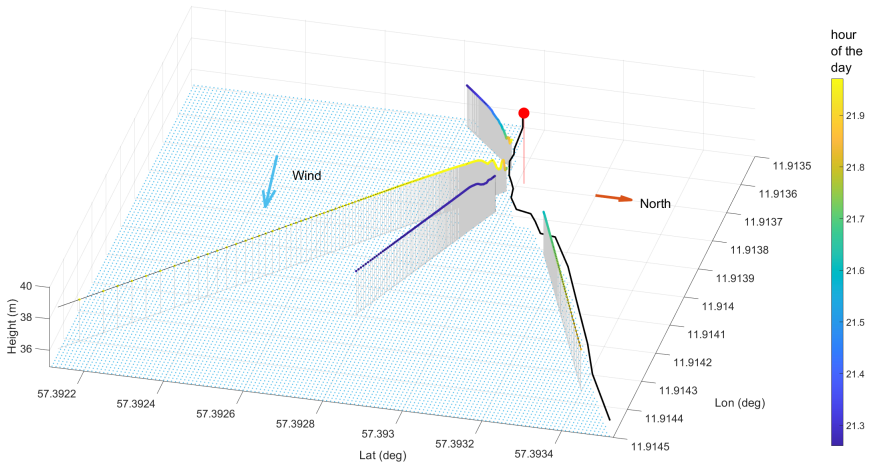

Figure 24: Observed heights for different specular points, courtesy *Mostafa Hoseini*.

tion of the specular points can also play a role. Figure 27 show the reflection

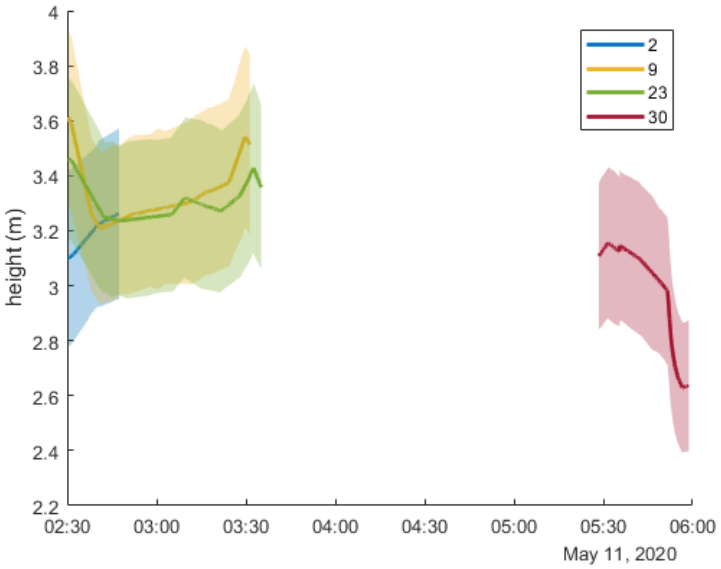

Figure 25: Heights estimated from cross-polar signal reflected off the ocean surface on 11.05.2020. We observe that we do not have satellites available for reflection events at all times.

points for these satellites. We can observe that both satellites have these points close to the edge of the coastline. Furthermore, both satellites have their reflections over the land or shallow waters. The significance of these factors should be considered further for optimization of the area used for specular reflection. This is however not done in this thesis.

It worth noting that the gradient of the heights are at times vastly different from the expected behavior. The sudden jumps in value are caused by the inaccurate period estimates found in the wavelet analysis. Figure 28 shows the periods observed for PRN 10. We observe that several large jumps occur. Furthermore, we can observe that these jumps occur due to the lack of a strong, coherent response. The lack of a strong response also increase the likelihood of the observed period providing erroneous heights, as we would not be able to retrieve the correct period. In the final height computations, the impact of such observations will be suppressed by the weighting utilizing the power ratios and the satellite elevation angle. However, due to the issues of redundancy in the observations, such errors can still have a large impact on the results. In the case of having enough observations these observations

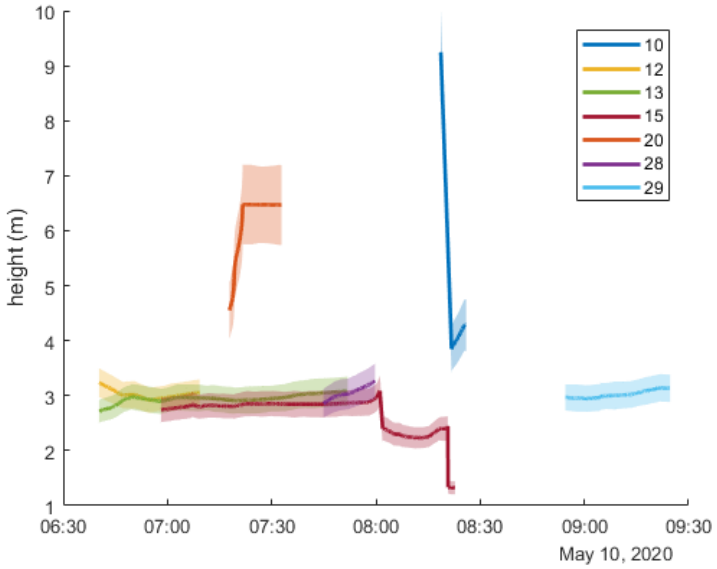

Figure 26: Heights computed from cross-polar reflection on 10.05.2020.

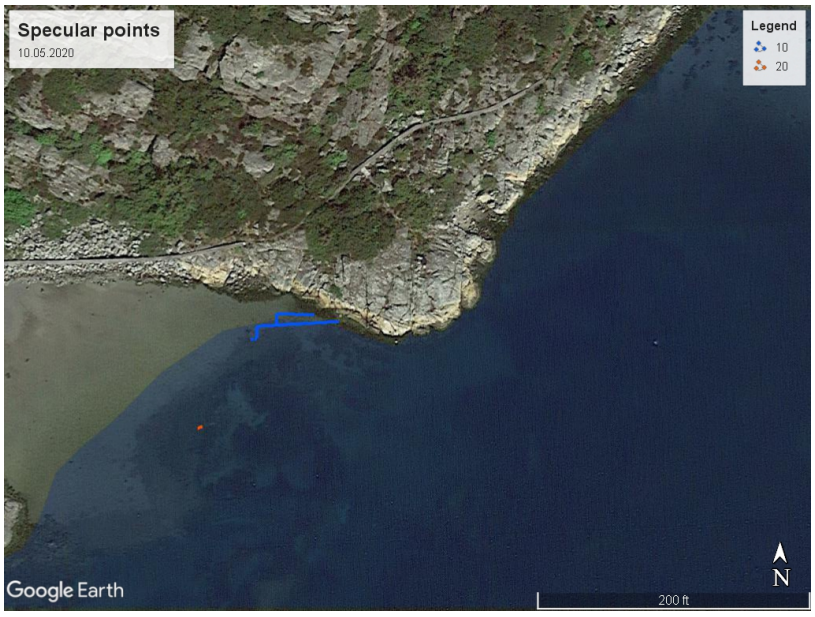

Figure 27: Specular points estimated for PRN 10 and 20.

can be treated as outliers and removed from the final height estimations.

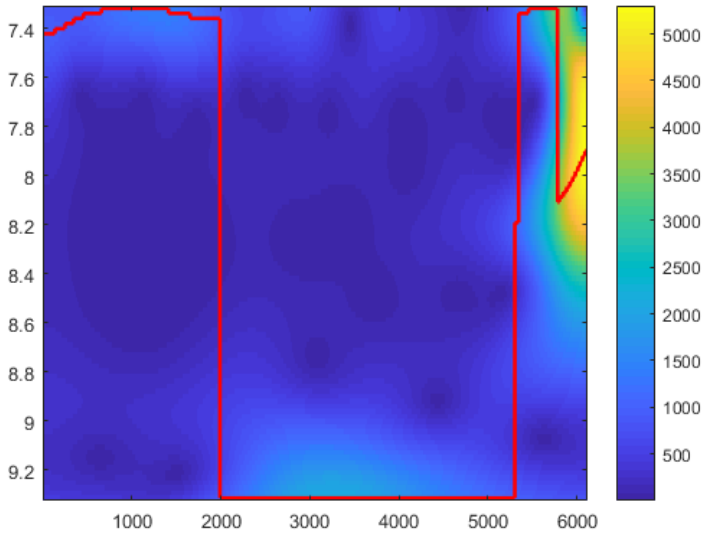

Figure 28: Significant periods of PRN 10 on 10.05.2020. We observe a large jump in the observed significant period.

The errors steming from orbital information of the satellites should be considered specially when the frequency of interferometric oscillations are used for height estimation. To check the expected visibility and poisition of satellites during the observation intervals, the online GNSS planning tool by Trimble, which can be found at `https://www.gnssplanning.com/`, was used. Figure 29 show a snapshot of the satellites over the horizon for the receiver at the start of the observation period. The distance from the center of the circle shows the elevation angle, while the angle in the circle shows the azimuth angle. The green lines show the trajectory of the satellites. Liu et al. [2017] found an appropriate range of azimuth angles to be from 75 to 225 degrees. Additionally, we have set the constraint to only consider satellites with elevation angles in the range of 3 to 40 degrees. Based on these restrictions, we can observe that the satellites used in height computations are within the expected limits in the sky plot. The satellites used in producing the time series are moving towards the area which can provide good reflection events. The elevation angles also coincide with the expected values as PRN

18 and 21 have a large elevation angle and they are moving out of the valid range.

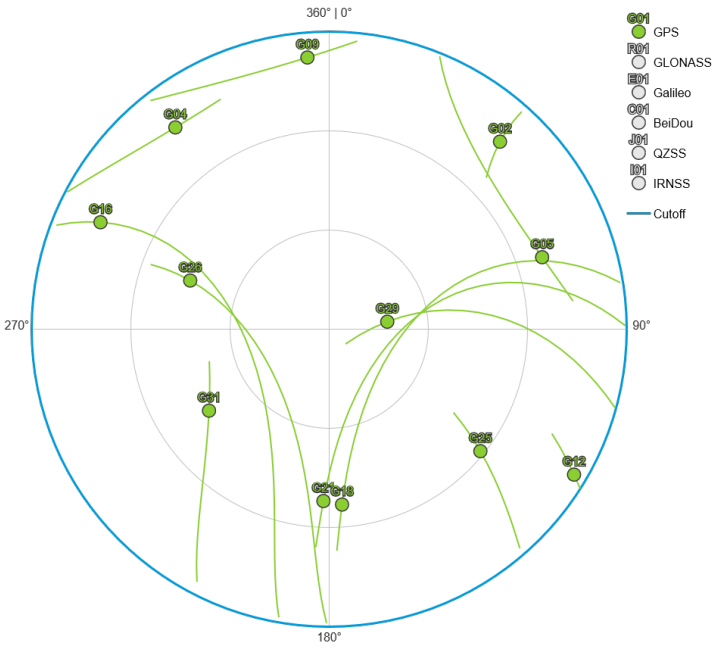

Figure 29: Satellite visibility from the online Trimble GNSS planning tools. The timestamp is set to 09.05.2020 12:30

For the purposes of satellite availability, from Figures 22 and 25 we can observe that there are at time few or even no satellites which can be used for reflectometry. In its current implementation this poses as a serious drawback as we wish for a system which can provide sea level heights in real time. The described system only utilises the L1 signal of the GPS satellites. The robustness and availability of the computed heights could therefore be increased by utilizing the other GNSS services, such as GLONASS, Galileo and BeiDou.

5.2 Height Anomaly Determination

Figure 30 shows the height anomalies computed using the method described in Section 4.3 from the satellites shown in Figure 22 compared to the anomalies computed by the tide gauge data from Onsala. We observe from the

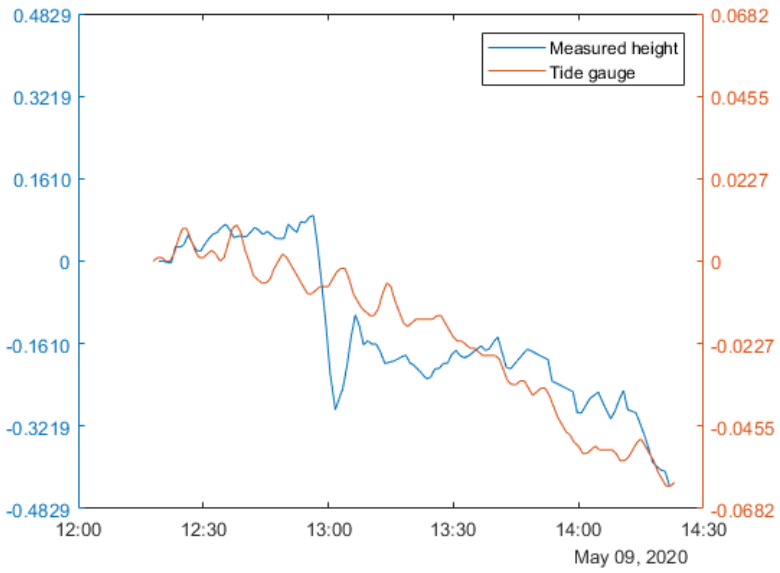

Figure 30: Height anomalies in meters for 09.05.2020

figure that the satellite height anomaly follows the trend of the tide gauge data. This is a promising since the observed trend of the sea level is in agreement with the tide gauge data despite utilizing low precision observations from standard messages of the receiver. If we compare the computed height anomalies to the individual heights computed from satellites in Figure 22, we can observe that the general trend of the satellites and the height anomalies largely coincide. Additionally, we can observe that PRN 18, 21 and 29 have less of an impact on the height anomalies, which is to be expected since their worsening impact is suppressed by the utilized weighting policy.

However, it is important to note the difference in scale between the anomalies. The tide gauge records a difference of around $7cm$ over the time period, while the satellites record a difference of almost $50cm$. Figure 31 Show the anomalies computed from the satellites from Figure 26. We can observe the same phenomenon, where the trend is similar, but the scale is

larger for the satellites compared to the tide gauge.

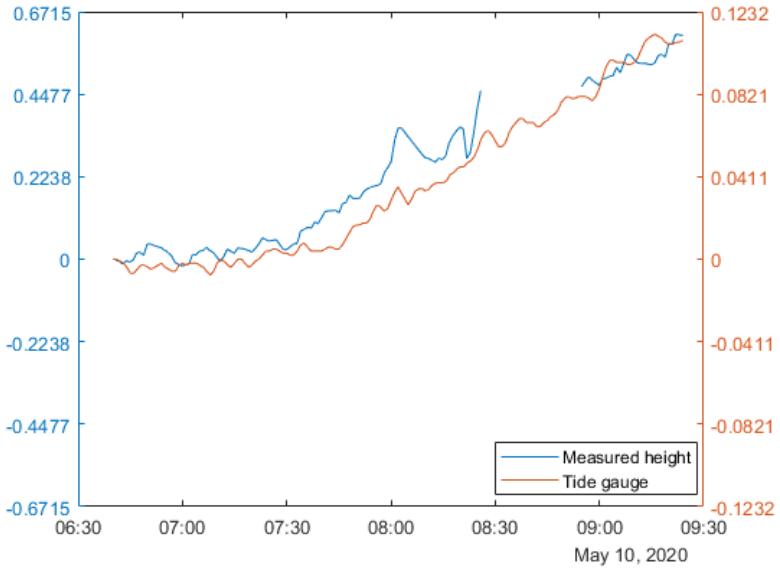

Figure 31: Height anomalies in meters for 10.05.2020

The satellites having larger values are to be expected due to the nature of the observations. As we are using the orbit information broadcasted by the satellites. The errors introduced by these observables greatly increase the expected values of the height anomalies.

Figure 32 shows a computed time series where the trend does not fit as well as the previous figures. We still observe similar tendencies regarding scale, and observe that subsets of the time series may coincide although the general trend is erroneous. Several factors may contribute to these discrepancies. First, recall that we may have time periods with low redundancy. The impact errors would have on our final height anomaly estimation would therefore be increased.

Table 3 Shows the correlations between the tide gauge and computed height anomalies. Additionally, both wind speed and direction is listed. From the table we can observe that while for some data sets we have significant positive correlation, such as for datasets 1 and 3, we also have datasets in which we do not have this property. We can observe that the wind speed alone does not necessarily affect how well the observed heights fit the tide

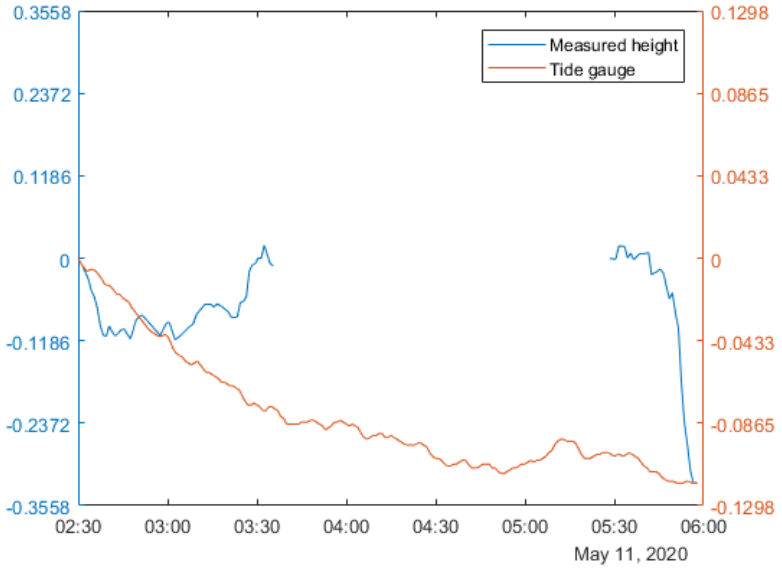

Figure 32: Height anomalies in meters for 11.05.2020

gauge data. We would expect to associate a larger wind speed with a decrease in fit due to the increase in the BCRS expressed by Equation 15. However, we can also observe from the equation that the BCRS is dependent on the mean square slope along and across the wind direction. We would therefore assume that the wind direction would significantly affect the quality of the reflected signal. From the table, we can observe that the datasets with the best correlation have similar direction of the wind. Furthermore, the two datasets which has seemingly random behavior compared to the tide gauge has a wind direction moving close to directly towards or away from the coast at Onsala. It is however important to note that there is a limit on the number of datasets used in this thesis, and we therefore cannot draw any general conclusions regarding the effect of wind speed and direction on the computed heights. This effect should be further investigated in future research.

5.3 Evaluation of Errors

Equation 27 enables us to estimate the errors of the results given the errors in our observables. As previously mentioned, values for these errors were obtained by using precise orbit information. It is however important to un-

Table 3: Correlation between tide gauge anomalies and computed height anomalies

Date	Span	wind speed (m/s)	direction (degrees)	Correlation
09.05.2020	12:15 - 14:25	4.267	221.00	0.8442
09.05.2020	17:40 - 20:10	3.000	206.75	0.1020
10.05.2020	06:40 - 09:30	6.650	216.75	0.9716
11.05.2020	02:30 - 06:00	9.925	10.25	-0.0799
12.05.2020	00:40 - 03:20	5.600	263.50	-0.4126

derstand the impact that the errors in these observables will have on the computed heights. Figure 33 shows how the error varies over different elevation angles. We observe that an increase in elevation angle increases the expected error, given that only the elevation angle varies, where the total error varies between 32 and 42 cm. This is to be expected, and has previously been discussed and taken into account. For the further analysis, we consider an elevation angle of 20 degrees with an estimated error of 34.3cm.

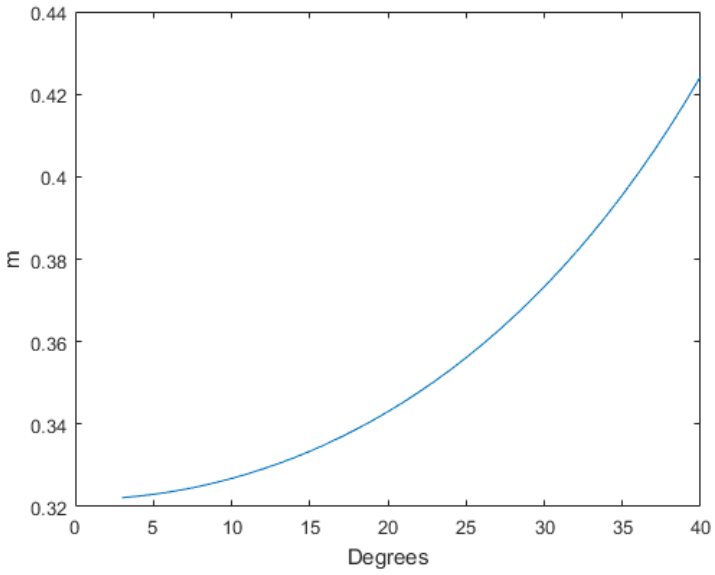

Figure 33: Error of heights for varying elevation angles

It is also important to evaluate the impact of each error contributor. To evaluate the impact, errors are computed for values around the expected

values used previously. When considering an error of an observable, the other errors are neglected. Figure 34 shows the magnitude of the error given different elevation angle errors. Compared to the total error from Figure 33, we can observe that an increase in the elevation angle would not increase the total error by more than a couple of cm, with a value of $2.15cm$ with an elevation angle error of 1 degree. Additionally, we can observe an error of $0.64cm$ around the expected value of 0.3 degrees.

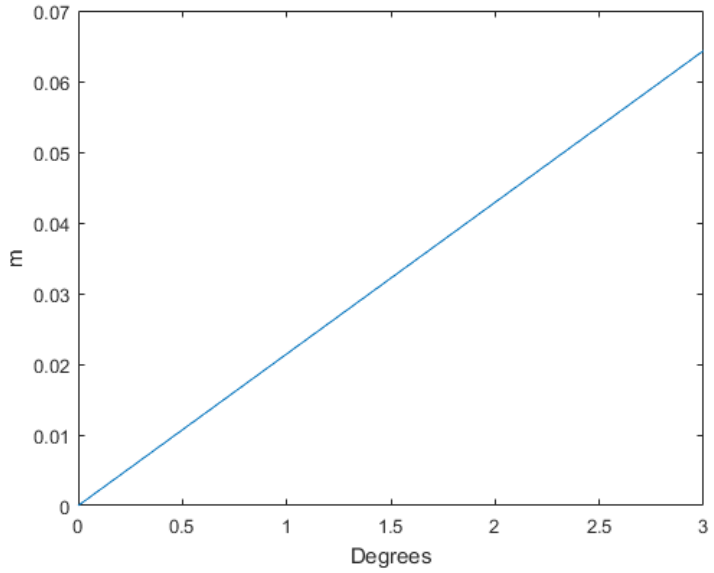

Figure 34: Contribution from elevation angle error

If we however consider the errors in the elevation angle rate, we can see the importance of having precise information regarding the elevation angles. Figure 35 shows the contribution of elevation angle and the impact of change in this error. We observe the contribution of this error is much larger compared to the elevation angle itself, providing an error of $33.77cm$ around the expected value of $1e-5rad/s$.

Lastly, we can consider the impact of the error in the observed period. Figure 5.3 show the contribution from the period error given a varying error. We observe that the contribution from the period error is larger than the error of the elevation angle, but significantly lower than the error of the elevation angle rate, with an error of $5.63cm$ at the expected error of $5s$.

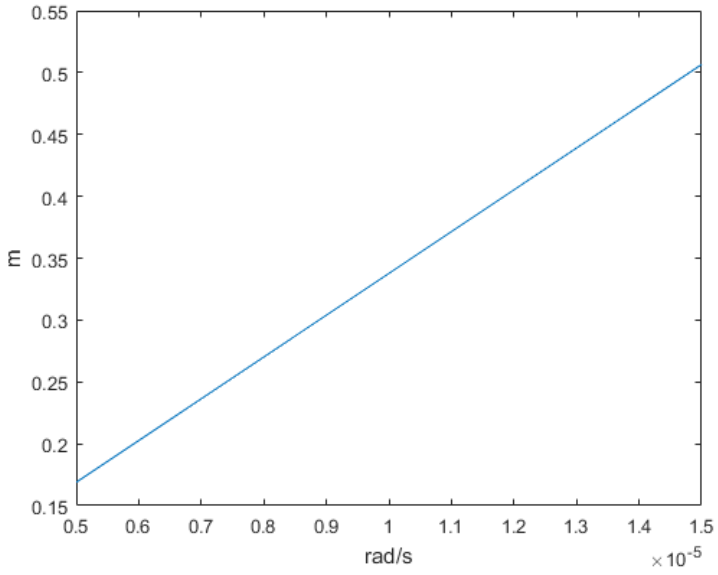

Figure 35: Contribution from elevation angle rate error

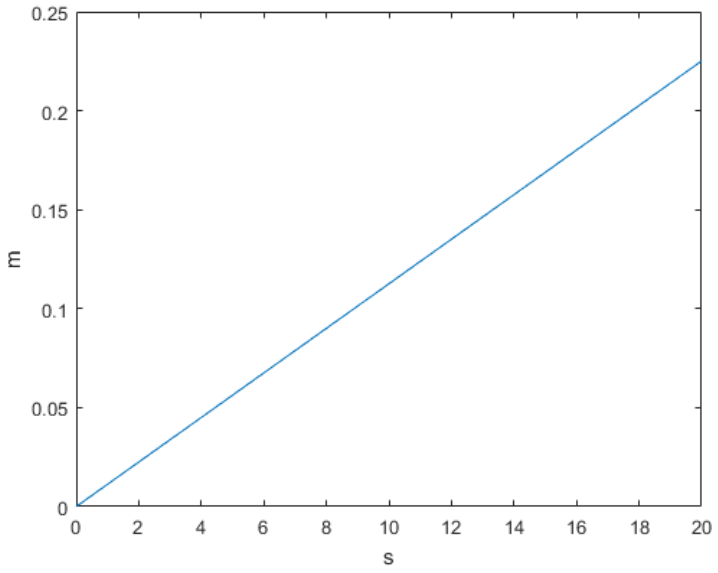

Figure 36: Contribution from period error

From these figures we can observe that the heights are very sensitive to variations in the elevation angle rate. The contribution of the elevation angle rate is also the most significant of the errors. The greatest reduction in error would therefore be achieved by reducing this error. As previously mentioned, this is often achieved by using ultra-rapid orbit information predicted by IGS, which provides more precise information than the broadcast ephemeris used in this thesis. By using the real-time predicted half-orbit data released by IGS, the satellite orbit accuracy could be drastically reduced from an accuracy of around $100cm$ to around $5cm$ (the satellite position in the orbit) [IGS, 2020]. We can however expect that a reduction in these errors would potentially greatly improve the results. The contribution of the elevation angle error would also be reduced, which while not as significant as the rate would also help improving the results.

For the error in period, we can observe that a large error in observation could be caused for a significant amount of error. From the wavelet analysis, we have observed that our computed height may contain large errors originating from the observed period due to a low correlation response at a given lag. This gross error can be alleviated by using the low power ratio at this time period in the weighting factor. However, we have observed that these errors may also have a significant impact on the final height estimate whenever the number of redundant observations are low. While the error in the period can be slightly reduced by decreasing the steps of periods within the wavelet analysis, gross errors caused by the observed period would be greatly reduced by increasing the number of concurrent measurements by utilizing observations from multi-GNSS satellites.

6 Conclusion

In this thesis, the feasibility of real-time estimation of sea surface height using the reflected signals of Global Navigation Satellite System (GNSS) was demonstrated. The interferometric oscillations originating from the interaction of the reflected and direct signals can be observed in the received signal power and were considered here as our main observable. We applied the interferometric GNSS-Reflectometry (GNSS-R) technique to the stand-alone high-rate data stream from a coastal experiment at Onsala space observatory, Sweden. A software package was developed to handle 200Hz observations from a GNSS occultation, reflectometry, and scatterometry receiver (GORS) at the station and to produce the time series required for the height retrieval processing. We used combination of singular spectrum analysis (SSA) and wavelet transform method for the height retrieval. The analysis shows promising results as well as highlighting the limitations of the utilized observations and approach.

The measurements retrieved from satellites at lower elevation angles exhibit favorable behavior for the altimetry application. This is owing to the reduced impact of sea surface roughness at low elevation angles which in turn results in stronger reflections. During the periods in which multiple satellites were in view, the retrieved sea level anomalies can reflect the trend of height variations. Therefore, one of the limitations present in the current implementation is the satellite availability. For several intervals, we were able to use only one satellite. Moreover, we were not able to guarantee having satellites available at all times. Another issue would raise during the periods in which the interferometric signal strength is weak, and as a result the height retrieval faces difficulties. This could happen during high wind speeds or for the reflection with higher elevation angles.

The error analysis shows that the issue of orbital information accuracy can make a significant contribution to the overall error budget, where the information about the rate of change for the satellite elevation angle is the greatest contributor.

6.1 Future Work

As previously outlined, the errors identified in this thesis can be reduced through different measures. Methods for improving the implementation would be to increase the number of satellites by utilizing the constellations of for example GLONASS and Galileo. This would increase the redundancy of the height retrievals by concurrent observations computed heights and improve the overall quality of the results. Additionally, introducing the real-time predicted half-orbits from IGS processing centers rather than the broadcast ephemeris would further improve the estimated rate of changes for the elevation angle and enhance the quality of the height anomalies.

Further work could also be focused on the ability to perform real-time height anomaly computation by reading data streamed directly from a receiver rather than recorded files stored locally. While the current implementation is simulating reading the data streamed from a receiver and process its data, it does not perform both the reading of receiver data stream and processing of this data at the same time. In the interest of moving towards a real-time altimetry service using reflectometry, the entire process should be streamlined into a single, continuous process which is capable of providing height estimates while receiving updates from the receiver. Lastly, a future research could also explore to a greater degree the effect of the wind speed and wind direction on the observations.

References

Georg Beyerle. Carrier phase wind-up in gps reflectometry. *GPS Solutions*, 13, 12 2008. ISSN 1521-1886. doi: 10.1007/s10291-008-0112-1. URL https://doi.org/10.1007/s10291-008-0112-1.

Estel Cardellach, Fran Fabra, Oleguer Nogués-Correig, Santi Oliveras, S. Ribó, and A. Rius. Gnss-r ground-based and airborne campaigns for ocean, land, ice, and snow techniques: Application to the gold-rtr data sets. *Radio Science - RADIO SCI*, 46, 12 2011. doi: 10.1029/2011RS004683.

Ian Cooper. Fdtd electromagnetic wave simulations of propagating waves incident upon a boundary between two non-magnetic and non-lossy uniform dielectric media. http://www.physics.usyd.edu.au/teach_res/mp/doc/EHs03.htm, 2013. Accessed 19.03.2020.

Brian Dunbar and Bob Allen. Cygnss overview. https://www.nasa.gov/cygnss/overview, 2017. Accessed 13.02.2020.

Bernd Eissfeller and Jong-Hoon Won. *Receiver Architecture*, pages 365–400. Springer International Publishing, Cham, 2017. ISBN 978-3-319-42928-1. doi: 10.1007/978-3-319-42928-1_13. URL https://doi.org/10.1007/978-3-319-42928-1_13.

US Air Force. https://www.gps.gov/systems/gps/space/, 2 2020a. Accessed 15.04.2020.

US Air Force. New civil signals. https://www.gps.gov/systems/gps/modernization/civilsignals/, 2 2020b. Accessed 27.02.2020.

James L. Garrison and Stephen J. Katzber. Effect of sea roughness on bistatically scattered range coded signals from the global positioning system. *Geophysical Research Letters*, 25:2257–2260, 1998.

JAVAD GNSS. Greis: Gnss receiver external interface specification. http://download.javad.com/manuals/GREIS/GREIS_Reference_Guide.pdf, 3 2020.

Nina Golyandina and Anatoly Zhigljavsky. *Basic SSA*, pages 11–70. Springer Berlin Heidelberg, Berlin, Heidelberg, 2013. ISBN 978-3-642-34913-3. doi: 10.1007/978-3-642-34913-3_2. URL https://doi.org/10.1007/978-3-642-34913-3_2.

NAVSTAR GPS. Global positioning system, standard positioning service, signal specification. https://www.gps.gov/technical/ps/1995-SPS-signal-specification.pdf, 06 1995.

GSA. https://www.gsa.europa.eu/european-gnss/galileo/galileo-european-global-satellite-based-navigation-system, 5 2019. Accessed 15.04.2020.

Ned Horning. Remote sensing. In Sven Erik Jørgensen and Brian D. Fath, editors, *Encyclopedia of Ecology*, pages 2986 – 2994. Academic Press, Oxford, 2008. ISBN 978-0-08-045405-4. doi: https://doi.org/10.1016/B978-008045405-4.00237-8. URL http://www.sciencedirect.com/science/article/pii/B9780080454054002378.

Mostafa Hoseini, Fadwa Alshawaf, Hossein Nahavandchi, Galina Dick, and Jens Wickert. Towards a zero-difference approach for homogenizing gnss tropospheric products. *GPS Solutions*, 24, 11 2019. doi: 10.1007/s10291-019-0915-2. URL https://doi.org/10.1007/s10291-019-0915-2.

Mostafa Hoseini, Milad Asgarimehr, Valery Zavorotny, Hossein Nahavandchi, Christopher Ruf, and Jens Wickert. First evidence of mesoscale ocean eddies signature in gnss reflectometry measurements. *Applications of GNSS Reflectometry for Earth Observation*, 2020. doi: 10.3390/rs12030542.

IAC. https://www.glonass-iac.ru/en/guide/index.php, 2020. Accessed 15.04.2020.

IGS. http://www.igs.org/products, 2020. Accessed 01.06.2020.

Shuanggen Jin, Estel Cardellach, and Feiqin Xie. *GNSS Remote Sensing: Theory, Methods and Applications*. Springer Netherlands, Dordrecht, 2014. ISBN 978-94-007-7482-7. doi: 10.1007/978-94-007-7482-7. URL https://doi.org/10.1007/978-94-007-7482-7.

Hyunglok Kim and Venkat Lakshmi. Use of cyclone global navigation satellite system (cygnss) observations for estimation of soil moisture. *Geophysical Research Letters*, 45(16):8272–8282, 2018. doi: 10.1029/2018GL078923. URL https://agupubs.onlinelibrary.wiley.com/doi/abs/10.1029/2018GL078923.

Kristine M. Larson, Eric E. Small, Ethan D. Gutmann, Andria L. Bilich, John J. Braun, and Valery U. Zavorotny. Use of gps receivers as a soil moisture network for water cycle studies. *Geophysical Research Letters*, 35(24), 2008. doi: 10.1029/2008GL036013. URL https://agupubs.onlinelibrary.wiley.com/doi/abs/10.1029/2008GL036013.

Hsueh-Jyh Li and Yean-Woei Kiang. 10 - radar and inverse scattering. In WAI-KAI CHEN, editor, *The Electrical Engineering Handbook*, pages 671 – 690. Academic Press, Burlington, 2005. ISBN 978-0-12-170960-0. doi: https://doi.org/10.1016/B978-012170960-0/50047-5. URL http://www.sciencedirect.com/science/article/pii/B9780121709600500475.

Wei Liu, Jamila Beckheinrich, Maximilian Semmling, Markus Ramatschi, Sibylle Vey, Jens Wickert, Thomas Hobiger, and Rüdiger Haas. Coastal sea-level measurements based on gnss-r phase altimetry: A case study at the onsala space observatory, sweden. *IEEE Transactions on Geoscience and Remote Sensing*, 55(10):5625–5636, Oct 2017. ISSN 1558-0644. doi: 10.1109/TGRS.2017.2711012.

Thuy Mai. Global positioning system history. https://www.nasa.gov/directorates/heo/scan/communications/policy/GPS_History.html, 2012. Accessed 14.02.2020.

Manuel Martin-Neira. A passive reflectometry and interferometry system (paris): Application to ocean altimetry. *ESA Journal*, 17:331–355, 01 1993.

Item Media. Antenna fundamentals. https://interferencetechnology.com/antenna-fundamentals/, 2007. Accessed 25.03.2020.

Mikhail Samoilovich Neiman. The principle of reciprocity in antenna theory. *Proceedings of the IRE*, 31(12):666–671, 1943.

Felipe G. Nievinski and Kristine M. Larson. Forward modeling of gps multipath for near-surface reflectometry and positioning applications. *GPS Solutions 18(2)*, pages 309–322, 2014.

Clement A. Ogaja. *Applied GPS for Engineers and Project Managers*. American Society of Civil Engineers, 2011. doi: 10.1061/9780784411506. URL `https://ascelibrary.org/doi/abs/10.1061/9780784411506`.

Kirill Palamartchouk, Peter J. Clarke, Stuart J. Edwards, and Rajesh Tiwari. Dual-polarization gnss observations for multipath mitigation and better high-precision positioning. *Proceedings of the 28th International Technical Meeting of the Satellite Division of The Institute of Navigation (ION GNSS+ 2015)*, pages 2772–2779, 9 2015.

Antonio Rius and Estel Cardellach. *Reflectometry*, pages 1163–1186. Springer International Publishing, Cham, 2017. ISBN 978-3-319-42928-1. doi: 10.1007/978-3-319-42928-1_40. URL `https://doi.org/10.1007/978-3-319-42928-1_40`.

Nereida Rodriguez Alvarez, Xavi Bosch, Adriano Camps, Mercè Vall-llossera, E. Valencia, Juan Marchan, and Isaac Ramos-Perez. Soil moisture retrieval using gnss-r techniques: Experimental results over a bare soil field. *Geoscience and Remote Sensing, IEEE Transactions on*, 47:3616 – 3624, 12 2009. doi: 10.1109/TGRS.2009.2030672.

Christopher Ruf, Derek Posselt, Sharanya Majumdar, Scott Gleason, M.P. Clarizia, Derek Starkenburg, Damen Provost, Valery Zavorotny, John Murray, Stephen Musko, Zorana Jelenak, Paul Chang, and Mary Morris. *CYGNSS Handbook*. Michigan Publishing, 04 2016. ISBN 978-1-60785-380-0.

Christopher Ruf, Clara Chew, Timothy Lang, Mary G. Morris, Kyle Nave, Aaron Ridley, and Rajeswari Balasubramaniam. A new paradigm in earth environmental monitoring with the CYGNSS small satellite constellation. *Scientific Reports*, 8, 2018. doi: 10.1038/s41598-018-27127-4.

Rui Sarnadas. Front end. `https://gssc.esa.int/navipedia/index.php/Front_End`, 2011. Accessed 23.03.2020.

Maximilian Semmling, Anja Rösel, Amitry V. Divine, Sebastian Gerland, Georges Stienne, Serge Reboul, Marcel Ludwig, Jens Wickert, and Harald Schuh. Sea-ice concentration derived from gnss reflection measurements in fram strait. *IEEE Transactions on Geoscience and Remote Sensing*, 57 (12):10350–10361, Dec 2019. ISSN 1558-0644. doi: 10.1109/TGRS.2019.2933911.

Roghayeh Shamshiri, Hossein Nahavandchi, and Gholamreza Joodaki. Seasonal variation analysis of greenland ice mass time-series. *Acta Geodaetica et Geophysica*, 3 2018. doi: 10.1007/s40328-017-0198-4. URL https://doi.org/10.1007/s40328-017-0198-4.

David Stephenson. Singular spectrum analysis. https://folk.uib.no/ngbnk/kurs/notes/node124.html, 9 2009. Accessed 27.04.2020.

Jaume Sanz Subirana, Jose Miguel Juan Zornoza, and Manuel Hernández-Pajares. Antenna phase centre. https://gssc.esa.int/navipedia/index.php/Antenna_Phase_Centre, 2011. Accessed 23.03.2020.

Devaraj Suresh and Kiran Yarrakula. Insar based deformation mapping of earthquake using sentinel 1a imagery. *Geocarto International*, 0(0):1–10, 2019. doi: 10.1080/10106049.2018.1544289. URL https://doi.org/10.1080/10106049.2018.1544289.

John C. Toomay. *Radar Cross Section*, pages 65–81. Springer Netherlands, Dordrecht, 1989. ISBN 978-94-011-6985-1. doi: 10.1007/978-94-011-6985-1_4. URL https://doi.org/10.1007/978-94-011-6985-1_4.

Valery Zavorotny, Scott Gleason, Estel Cardellach, and Adriano Camps. Tutorial on remote sensing using gnss bistatic radar of opportunity. *IEEE Geoscience and Remote Sensing Magazine*, 2(4):8–45, Dec 2014. ISSN 2373-7468. doi: 10.1109/MGRS.2014.2374220.

Alireza Zolfaghari. *Receiver Front End*, pages 41–55. Springer US, Boston, MA, 2003. ISBN 978-1-4757-3787-5. doi: 10.1007/978-1-4757-3787-5_4. URL https://doi.org/10.1007/978-1-4757-3787-5_4.

NTNU

Norwegian University of
Science and Technology